

Impact of dynamics, entanglement, and Markovian noise on the fidelity of few-qubit digital quantum simulation

Max D. Porter and Ilon Joseph

Fusion Energy Sciences Program, Lawrence Livermore National Laboratory
June 9, 2022

For quantum computations without error correction, the dynamics of a simulation can strongly influence the overall fidelity decay rate as well as the relative impact of different noise processes on the fidelity. Theoretical models of Markovian noise that include incoherent Lindblad noise, gate-based errors, and stochastic Hamiltonian noise qualitatively agree that greater diffusion and entanglement throughout Hilbert space typically increase the fidelity decay rate. Simulations of the gate-efficient quantum sawtooth map support these predictions, and experiments performed on three qubits on the IBM-Q quantum hardware platform at fixed gate count qualitatively confirm the predictions. A pure depolarizing noise model, often used within randomized benchmarking (RB) theory, cannot explain the observed effect, but gate-based Lindblad models can provide an explanation. They can also estimate the effective Lindblad coherence times during gates, and find a consistent $2\text{--}3\times$ shorter effective T_2 dephasing time than reported for idle qubits. Additionally, the observed error per CNOT gate exceeds IBM-Q's reported value from RB by $3.0\times$ during localized dynamics and $4.5\times$ during diffusive dynamics. This demonstrates the magnitude by which RB understates error in a complex quantum simulation due to dynamics and crosstalk.

1 Introduction

1.1 Motivation

Quantum computers may eventually become indispensable to scientific computing due their ability to accelerate many calculations of interest. While achieving this goal will require error correction, the noisy intermediate scale quantum (NISQ) devices that are available today provide a unique platform for exploring the dynamics of many-body quantum systems. The ubiquitous presence of interactions with the environment generates noise which adds complexity to the interpretation of the results. Depending on context, noise can affect the dynamics in different ways. It may completely wash out the dynamics of interest or it can potentially be used to measure key signatures of the dynamics [1]. In this work we ask the question: how does the dynamics influence the effects of noise? We show that varying the dynamics of a chaotic quantum map alters the fidelity decay due to noise in three different noise models, and demonstrate that these effects are observable today using experiments on the IBM-Q Quantum Lab.

Quantum simulation is one of the main applications of interest for achieving near term quantum advantage [2]. Simulating chaotic dynamics is of particular interest due to the provable difficulty of simulating chaos. Recent claims of quantum supremacy relied on the difficulty of simulating chaotic quantum circuits [3, 4] and among paths to quantum advantage simulating chaotic dynamics may be the most qubit-efficient [5]. Measuring the decay of fidelity can also provide an exponentially efficient measure of the classical Lyapunov exponent [6, 7] and chaotic decoherence [8]. Measuring dynamical localization of classically chaotic systems may yield a similar speedup [9]. The fidelities of quantized versions of classically chaotic Hamiltonian sys-

arXiv:2206.04829v1 [quant-ph] 10 Jun 2022

Max D. Porter: porter42@llnl.gov

tems can decay differently (often faster) than for integrable dynamics [10, 11, 1]. Quantum chaos can magnify the effect of Trotter errors [12] while quantum localization can bound Trotter errors [13].

Both chaotic diffusion and dynamical localization can be observed in the quantum sawtooth map, which also has a particularly efficient algorithm for running on gate-based quantum devices. The transition from diffusion to localization occurs when the ratio of diffusion strength to effective \hbar is small and quantum interference dominates. Refs. [14] and [15] initiated the use of the quantum sawtooth map to characterize experimental noise by using the degree of localization as a test of device fidelity. We extend this by studying the phase transition to diffusion and the Loschmidt echo fidelity throughout this transition, opening the door to probing the interaction between quantum map dynamics and experimental noise.

1.2 Summary of results

The main results are: (1) the dynamics being simulated affect the fidelity decay rate (2) due to the amount of entanglement and superposition that is generated. (3) Theoretical analysis quantifies how a randomly entangled state combines the effects of relaxation and dephasing errors, while (4) a gate-based Lindblad model can explain experimental observations and (5) allows one to measure effective T_1 and T_2 times for quantum gates. These effective coherence times more accurately describe the duration of complex quantum simulations, and the gate-based Lindblad model easily scales to many qubits.

The effect of the dynamics on the fidelity decay is demonstrated through theory, simulation, and experiment. The results of different noise models are compared via numerical fit in Sec. 4.2.2. The CNOT average error per gate for different dynamics is extracted from experiment and reported in Table 2. The effective T_1 and T_2 times are also extracted from the model fits and reported in Table 3.

Our gate-based dynamical Lindblad model has two main components. First, theoretical expressions are derived for the fidelity decay of a noisy Hamiltonian simulation during localized dynamics, chaotic/diffusive dynamics, and the middling case of unentangled superposition. (The term

diffusive dynamics will be preferred since the dynamics are not clearly chaotic until a sufficient number of qubits is used [1].) To derive these expressions, each type of dynamics is approximated as an appropriate steady state that gradually decoheres under Lindblad evolution. The resulting expressions reveal differing dependencies on the effective T_1 and T_2 times due to different degrees of random entanglement and superposition. The second component of this model is to connect it to the gate picture relevant to IBM-Q and many other platforms. Rather than qubits always decaying at a constant rate, they are assumed to decay more rapidly when acted on by a gate. On IBM-Q, the most error-prone gates are the two-qubit CNOT gates and, hence, we focus our attention on these gates alone. This retains the expected error dependence on the number of CNOT gates.

In reality errors come in many varieties not described by a Lindblad model. The most comprehensive description of Markovian gate errors requires gate set tomography [16, 17] to find a consistent set of process matrices for all gates. Yet the task of measuring all such processes is not scalable to many qubits and is not possible with the limited runtime on the open-access IBM-Q system. A reduced-order Lindblad model can still capture some of the key aspects of a process matrix better than the randomized benchmarking (RB) and single-qubit metrics currently used by IBM-Q. When a depolarizing process, e.g. determined by RB, is used to model the evolution [18], it provides errors that are independent of the density matrix (except for the fully mixed state), and hence the dynamics. Even the simplest Lindblad model captures more detail than this.

We briefly consider a stochastic error model that also predicts dynamics-dependent fidelity decay [19]. In this model a parameter of the Hamiltonian is perturbed stochastically during each discrete step of the chaotic quantum sawtooth map, though a static Hamiltonian perturbation model would have achieved a similar effect [20]. Parameter noise models correspond to lower-frequency noise that interacts more strongly with the dynamics, such as coherent error that varies from gate to gate, while fixed perturbation corresponds to zero frequency, namely static coherent error. Parameter noise

effects may be qualitatively similar to measured pink ($1/f$) noise dephasing processes [21]. Both types of noise predict an algebraic fidelity decay rate when the dynamics being simulated are localized, or more generally regular [19, 22, 1]. This is attributed to the slower separation of non-chaotic semiclassical path integral trajectories. However, through simulation we find this effect requires more than three qubits and so is not yet experimentally achievable with the quantum map and hardware used here. In the chaotic regime the parameter noise model also allows one to measure the Lyapunov exponent, though at least six qubits are required to observe it [6, 1]. We find that these parameter noise effects are compatible with the presence of Lindblad noise and might be observable in the near future.

1.3 Rationale for gate-based Lindblad model

Working with a complete decoherence model of quantum gates is quite challenging because there are many terms that are potentially active [23]. For a linear trace-preserving quantum process model, the number of terms is $N^4 - N^2$, where N is the number of states. Clearly, for all-to-all connectivity, a complete characterization is not scalable to many qubits.

Performing quantum process tomography [24] for a single entangling gate already requires a relatively large number of measurements. While there are software packages such as pyGSTi [16, 17] that allow one to automatically characterize a complete set of two-qubit gates, many of the commercial quantum hardware platforms available today do not allow enough run time to perform a complete characterization of even a single entangling gate. Moreover, because the complete protocol takes so long to run, the hardware characteristics may drift significantly over the duration of the experiments.

To make headway under such circumstances, one must attempt to utilize plausible simplifications of the number and types of decoherence processes under consideration. Assume that for each gate, one can identify a simplified set of decoherence processes that are dominant. One could then perform a restricted form of process tomography to characterize each gate. One could even characterize an entire gate set – assuming that the number of independent decoherence processes is small enough that this procedure is scalable.

Presumably, a detailed understanding of the physical processes that mediate decoherence mechanisms would yield a relatively concise mathematical description of the dominant decoherence processes. However, this could still potentially be quite complicated, for instance including non-Markovian processes, and would require custom experiments to diagnose and verify. Moreover, this could potentially require a physical model for the environment as well as for the quantum computing hardware, making the model non-Markovian and more complex than the process tomography paradigm typically admits.

Yet simply understanding the way that the physical system imposes a mathematical structure on the decoherence processes is potentially quite valuable. For example, theoretical studies have proven that the Lindblad master equation [23] is the appropriate infinitesimal generator of the temporal evolution of a quantum system coupled to an incoherent process that is both trace-preserving and completely positive. Hence, this implies that the Lindbladian form should be considered primary and that integrating the master equation over a finite time interval should be used to determine the associated process matrix. Clearly, a sparse representation in terms of Lindblad operators will typically yield a rather dense process matrix. Thus, from the physical perspective, it is much more likely for the Lindblad representation to be sparse than it is for the associated process matrix.

Another plausible physical assumption is that the dominant noise processes are from one- and two-qubit interactions. This reduces the number of processes exponentially, from $O(N^4)$ (the elements of the infinitesimal process matrix) when including up to all-qubit processes to just $O(\log^2(N))$ (the number of qubit pairs) for up to two-qubit processes. In the infinitesimal process matrix this corresponds to an exponential reduction in the number of elements. This can be seen by considering the relationship between the Lindblad equation, which describes the time evolution of the density matrix, and the infinitesimal process matrix, which describes the coupling of density matrix elements. Most process matrix elements of a large system couple density matrix elements between which more than two qubits have differing states. So limiting to one- and two-qubit processes treats most process matrix

elements as zero, leaving an exponentially small number of elements active.

Two-qubit processes could be further limited to fewer physically plausible channels. For instance photon exchange between qubits mediated by the environment could be an important channel, since it requires only one photon and is an extension of single-qubit relaxation and excitation processes [25]. A stronger restriction is limiting interactions to nearest neighbors in a sparsely connected device, reducing the number of processes to $O(\log(N))$. This also strengthens the assumption that no more than two-qubit processes need to be considered.

Two-qubit dephasing is a physically plausible channel that we found in our numerical studies to have very similar qualitative effects as the standard single-qubit dephasing. Presumably, the reason is that each multi-qubit dephasing process can be understood as single-qubit dephasing in an alternate basis. Understanding whether or not such non-standard dephasing terms are important for describing actual quantum hardware performance could be an interesting subject for future work.

The greatest physical simplification that can plausibly be applied to a Lindblad model is that only the single-qubit relaxation and dephasing processes are important, averaged over all qubits for simplicity, but that they are enhanced over their measured values during gate operation. (For typical quantum hardware platforms, the temperature is so far below the excitation energy that excitation processes can be considered subdominant.) While this may be a vast oversimplification, these processes are clearly important because they are universally required to model experimental data in practice. The physical meaning of this model is simple: the physical processes that actuate the gate renormalize the interaction between the qubit and the environment, and, hence, renormalize the characteristic single qubit relaxation and dephasing rates. Note, however, that the predictions are nontrivial because the associated time-integrated process matrix has a relatively dense form that depends on the products of the rates with the overall gate time.

While many other decoherence processes are likely needed for a truly accurate description of the quantum hardware evolution, we have found

that this simplest Lindblad model is sufficient for modeling the experimental data described in this work. Our work here has the restricted goal of attempting to determine the single-qubit decoherence enhancement for the CNOT gates that clearly dominate the IBM-Q error budget. Moreover, given the limited experimental data that one is able to obtain using today’s platforms, the data may not contain enough information to robustly determine additional free parameters over and above those contained in this simple model. In the future, it could be interesting to explore a more comprehensive approach to the determination of the relevant decoherence processes. Perhaps one could even attempt a version of gate set tomography [16] that deduces the relevant relaxation and dephasing enhancements for every qubit and every gate in the set.

1.4 Overview of contents

In Sec. 2.1 and Sec. 2.2 the quantum sawtooth map is introduced and the conditions for dynamical localization are described. In Sec. 2.3 the noise models under consideration are described in detail. Simplified analytical models are compared to numerical results and scaling with number of qubits is explored. Section 2.3.2 and Sec. 2.3.3 consider the Lindblad noise model, Sec. 2.3.4 considers the qiskit Aer noise model, and Sec. 2.3.5 considers the parameter noise model. Presented next is the implementation of the quantum sawtooth map as an algorithm. Sec. 3.1 gives its gate decomposition while Sec. 3.2 discusses the details of native gates, device connectivity, and gate depth scaling. In Sec. 4 experimental results are presented, compared to IBM-Q reported metrics, and fits using various models are performed. Lastly Sec. 5 provides a summary of our results.

2 Theoretical analysis

2.1 Quantum sawtooth map

The quantum sawtooth map (QSM) is defined by the time-periodic Hamiltonian

$$H_{QSM} = \frac{\hat{J}^2}{2} - \sum_n K \frac{\hat{\theta}^2}{2} \delta(t-n) \text{ for } \theta \bmod 2\pi \quad (1)$$

which is derived from the classical Hamiltonian by quantizing to get $\hat{J} = \hbar\hat{p}$ and discretizing to

get $\hat{\theta} = 2\pi\hat{q}/N$ to yield momentum and position operators \hat{p} and \hat{q} respectively, with eigenvalues $-N/2 \leq p, q < N/2$. The quantum evolution propagator over one period is then

$$\begin{aligned} U_{QSM} &= \hat{\mathcal{T}} e^{-i \int_0^1 H_{QSM} dt / \hbar} \\ &= U_{kin} U_{pot} \\ U_{pot}(\hat{q}) &= e^{ik(\beta\hat{q})^2/2} \\ U_{kin}(\hat{p}) &= e^{-i\hbar\hat{p}^2/2} \end{aligned} \quad (2)$$

where $\hat{\mathcal{T}}$ is the time-ordering operator, $k \equiv K/\hbar$ is the quantum kicking parameter, and $\beta \equiv 2\pi/N$ for N basis states. In the context of quantum computing $N = 2^n$ for n qubits. This single-period propagator is often called a Floquet operator, but since it corresponds to a classical map it is also known as a quantum map. Periodicity matching between the classical and quantum systems gives $\hbar = 2\pi L/N$ for positive integer L [1]. Note that when N is a power of two, making L even would allow L/N to simplify and reduce the pseudorandomness of the eigenphases of U_{pot} and U_{kin} , disrupting the chaotic dynamics, so L is assumed odd.

Note a partial symmetry between the phases of U_{kin} and U_{pot} : $\hbar = L * 2\pi/N$ while $-k\beta^2 = -K/L * 2\pi/N$. Typically the qubits are mapped to the p -basis, but mapping instead to the q -basis would swap the roles of L and $-K/L$.

2.2 Localization and initial conditions

When the classical diffusion coefficient D_K is small compared to \hbar^2 , the QSM is predicted after the Heisenberg time to reach a steady state that is exponentially localized around an initial momentum state $|p_0\rangle$ as

$$P_p = |\langle p | \psi \rangle|^2 \approx \frac{1}{\ell} e^{-\frac{2|p-p_0|}{\ell}} \quad (3)$$

with localization length [7]

$$\ell \approx D_K / \hbar^2. \quad (4)$$

The Heisenberg time or ‘‘break’’ time [7] is the time to resolve the energy levels, defined as the inverse mean energy level spacing [26, 27].

The presence of broken cantori in the classical system can slow diffusion at small K , so there are two regimes given by

$$D_K \approx \begin{cases} (\pi^2/3)K^2 & \text{for } K > 1 \\ 3.3K^{5/2} & \text{for } 0 < K < 1. \end{cases} \quad (5)$$

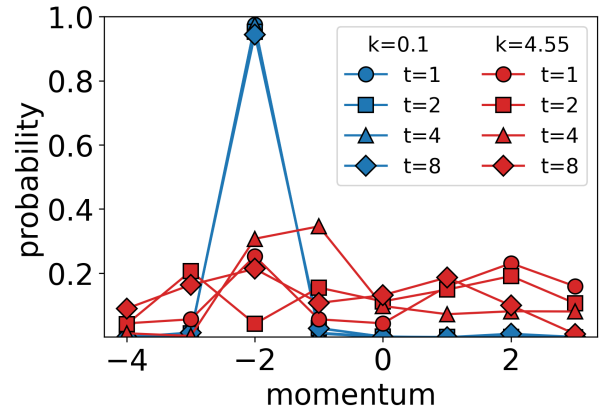


Figure 1: Exact noiseless simulations of the quantum sawtooth map (QSM), showing the localized case $k = 0.1$ (blue) and the diffusive case $k = 4.55$ (red) for $t = 1, 2, 4, 8$.

Due to the periodicity and finite size of the system, localization only occurs if the localization length is small enough to have a global maximum at its central peak. This occurs when

$$\begin{aligned} k &< k_{loc} \\ &\equiv \begin{cases} \sqrt{\frac{3}{\ln(2)\pi^2}} N \approx 0.66N^{1/2} & \text{for } K > 1 \\ \left(\frac{1}{3.3\sqrt{2\pi\ln(2)}} \frac{N^{3/2}}{L^{1/2}} \right)^{2/5} \approx 0.50N^{3/5}L^{-1/5} & \text{for } 0 < K < 1 \end{cases} \\ &= \max(0.66N^{1/2}, 0.50N^{3/5}L^{-1/5}) \end{aligned} \quad (6)$$

[1] with diffusion occurring otherwise. These two dynamical regimes are demonstrated in Fig. 1.

When localization is strong ($\ell \ll N$) the above formula for average ℓ does not uniformly apply to all initial conditions, with ℓ instead depending on initial condition in a manner dependent on L . Less localized groups of Floquet eigenstates appear at L equally spaced locations in momentum space, reducing ℓ for initial momentum states in the vicinity of these groups. Once $L \sim N$ this transitions to more uniform ℓ with just $|p=0\rangle$ strongly localized. This is how Refs. [14, 15] used $N = 8, L = 7$ to obtain strong localization at $|p=0\rangle$, despite other states being less localized. In this study we fix $L = 1$ to keep the state-dependent effect constant. When demonstrating strong localization in Fig. 1 we show a single $|p \neq 0\rangle$, while fidelity such as in Fig. 3 is averaged over all initial conditions to avoid state-dependent effects.

It is also worth noting that the initial con-

ditions are chosen to be momentum eigenstates rather than Floquet eigenstates. In the strongly localized limit, Floquet eigenstates are complex superpositions of $|p\rangle$ and $|-p\rangle$. As the quantum map causes the phase of each Floquet state to evolve at a rate proportional to its quasisenergy, pairs of states will fall out of phase, causing an initial state $|p\rangle$ to evolve to $|-p\rangle$ after a phase difference π . However, in the localized limit the quasienergies of these Floquet state pairs are close together, making this process long and irrelevant for the short time scales discussed in this paper. The fact that we reverse the map to calculate fidelity further reduces the relevance of this.

2.3 Noise models and fidelity

2.3.1 Types of noise and fidelities

Present day quantum devices are impacted by many different types of noise. This motivates studies of the types of noise that are present and how the errors impact algorithms of interest. On the IBM-Q platform errors occur primarily during two-qubit gates which in the QSM algorithm contribute about $10\times$ more to the total error over single-qubit gates, as discussed in Sec. 3.2. The types of error that occur may be incoherent Markovian relaxation and dephasing error (T_1 and T_2 respectively), coherent error, multi-qubit incoherent errors, or something else. Here three models of noise in a quantum map are considered for understanding the effects of errors: (1) A Lindblad master equation model of incoherent Markovian noise (both approximate theory and full simulation), (2) the IBM-Q Qiskit Aer gate-based Kraus simulator model of incoherent Markovian noise, and (3) a unitary parameter noise model of stochastic Hamiltonian error.

The overall impact of noise can be studied by its effect on the rate of fidelity decay of our quantum system. When the noise is unitary, such as parameter noise, with total evolution U_σ and noise amplitude σ , and a pure state $|\psi\rangle$ is used as an initial condition, the pure state fidelity is measured by

$$f(t) = |\langle\psi|U_{\sigma'}^{-t}U_\sigma^t|\psi\rangle|^2 \quad (7)$$

which is also known as the Loschmidt echo. σ' indicates the same magnitude as σ while being statistically independent. For non-unitary noise, such as Lindblad noise, one must use the more

general density matrix formulation

$$f(\rho, \sigma) = \left(\text{Tr} \sqrt{\sqrt{\rho}\sigma\sqrt{\rho}}\right)^2 \quad (8)$$

for ideal (initial) and noisy (final) density matrices ρ and σ , respectively. For an initial pure state $\rho = |\psi\rangle\langle\psi|$ this simplifies to

$$f = \langle\psi|\sigma|\psi\rangle \quad (9)$$

$$= \sum_{i,j} \langle\psi|i\rangle\langle i|\sigma|j\rangle\langle j|\psi\rangle = \sum_{i,j} \sigma_{i,j}\rho_{i,j}^* \quad (10)$$

Contrary to previous studies, noise here occurs during both forward and backward evolution, to connect simulation to experiment. This increases the physical time per map step by a factor of two, and therefore the observed fidelity decay rate by the same factor. In all cases we average the fidelity over the N computational basis state initial conditions $|p\rangle$ in order to study the average dynamics.

2.3.2 Effects of dynamics on Lindblad noise

The Lindblad master equation is the most general type of completely positive trace-preserving (CPTP) Markovian master equation. It can be written as

$$\frac{\partial\rho}{\partial t} = -i[H, \rho] + \sum_i \nu_i \left(L_i\rho L_i^\dagger - \frac{1}{2}\{L_i^\dagger L_i, \rho\} \right). \quad (11)$$

in dimensionless units where $t = t_{\text{phys}}/T_{\text{step}}$ has units in the number of map steps, $H = H_{\text{phys}}T_{\text{step}}/\hbar$, and $\nu_i = \nu_{i,\text{phys}}T_{\text{step}}$.

The time t describes forward-only noise, where ρ is evolved forward with Lindblad noise and then its fidelity is calculated by comparison to a noiseless evolution. In experiment this would require time-intensive full state tomography or a qubit-expensive swap test. Instead all results in this paper use forward-and-back time evolution in which ρ is evolved forward with noise and then backward ($H \rightarrow -H$) with a different realization of the noise. This doubles the physical time spent decohering per map step so that forward-and-back time $t_{\text{fb,phys}} = 2t_{\text{phys}}$ at the end of each map step. Converting this to map step time by $t_{\text{fb}} = t_{\text{fb,phys}}/(2T_{\text{step}}) = t$ results in a fidelity decay $f_{\text{fb}}(t_{\text{fb}})$ that is different from the forward-only fidelity $f(t)$. For many processes, like standard Lindblad decay, the doubled effect

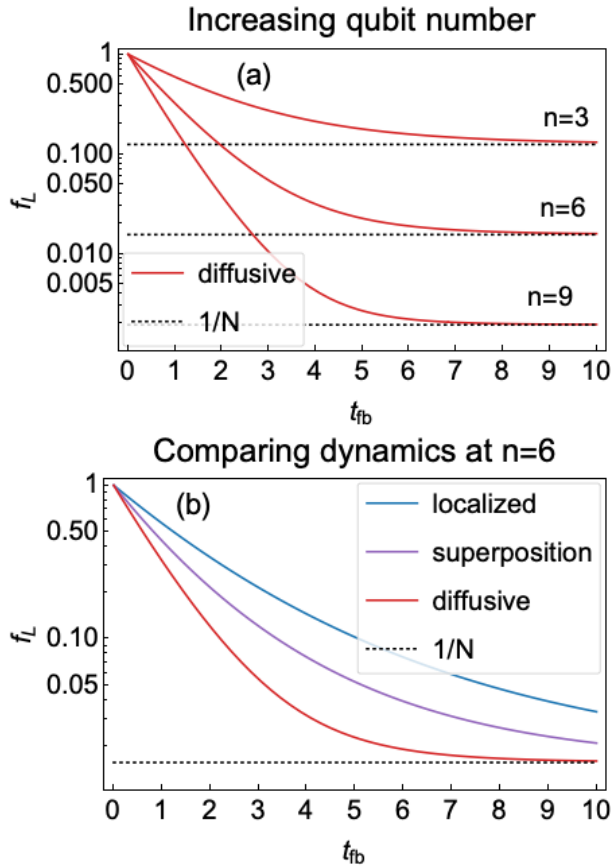


Figure 2: Theoretical Lindblad fidelity evolution for $\nu_1 = 0.1$ and $\nu_2 = 0.2$: (a) comparing the decay of a diffusive state for three, six, and nine qubits; (b) comparing the decay of localized, superposition, and diffusive states for six qubits. The average fidelity plateaus at the uniformly mixed limit $1/N$ when no information about the original state remains.

of noise doubles the decay rate per map step such that $f_{fb}(t_{fb}) = f(2t)$.

Equations in this paper still use forward-only time fidelity $f(t)$ for simplicity, but when comparing to simulations and experiment that use forward-and-back time and noise, $f(2t)$ is used. Parameter noise has an exception that limiting behaviors such as Lyapunov rate and algebraic rate decays appear to follow $f_{fb}(t_{fb}) \approx f(t)$ (see Sec. 2.3.5).

We use a simple model of unitary dynamics modified by the non-unitary decoherence processes of $2n$ single-qubit Lindblad operators L_i , causing relaxation to the ground state at rate ν_1 and pure dephasing at rate ν_2 for each qubit. These relate to relaxation time T_1 and total de-

phasing time T_2 via

$$\begin{aligned} 1/T_1 &= \nu_1 \\ 1/T_2 &= \nu_1/2 + \nu_2/2 \end{aligned} \quad (12)$$

as can be seen by comparing Appendix C to Ref. [28]. For calculating the fidelity, the ideal expected density matrix, which is also the initial density matrix, will be denoted ρ , and the noisy evolving density matrix will be denoted σ .

The main interaction between dynamics and Lindblad noise is that different types of dynamics have different typical density matrices that are influenced by each decoherence effect to different degrees. These include on-diagonal relaxation (of computational basis states), off-diagonal relaxation (of superpositions of basis states), and off-diagonal dephasing. In Appendix C, we analytically determine the decay of fidelity for pure states in the two dynamical limits of being highly localized and highly diffusive, as well as the case of uniform superposition, all three of which are summarized in this section. Briefly, the fidelity of localized pure states is affected only by on-diagonal relaxation due to their lack of off-diagonal terms, while the fidelity of diffusive pure states is affected only by off-diagonal relaxation and dephasing due to a cancellation of on-diagonal effects. The key finding here is that the ν_2 dependence differs between the two limiting cases, with a continuum of decay rates for the less localized or less entangled cases in between.

Starting with the fully localized case which has $k = 0$, initial conditions $|\psi\rangle = |p\rangle$ of computational basis states, and fidelity $f = \sigma_{p,p}$, the evolution of $|\psi\rangle$ due to the diagonal Hamiltonian has no effect on the density matrix σ and therefore on the fidelity. The Lindblad evolution acts alone, causing relaxation of each qubit towards the ground state at rate ν_1 . If one averages the fidelity over all possible initial states $|p\rangle$, the result is

$$f_L = \left(1 + e^{-2\nu_{\text{single}}t}\right)^n / 2^n \quad (13)$$

so that the initial effective decay rate is

$$\begin{aligned} f_L &\approx 1 - \nu_{\text{eff}}t + O(\nu_{\text{eff}}^2 t^2) \\ &\approx e^{-\nu_{\text{eff}}t} \end{aligned} \quad (14)$$

$$\nu_{\text{eff}} = n\nu_{\text{single}}$$

where

$$\nu_{\text{single}} = \nu_1/2 = 1/(2T_1) \quad (15)$$

for the localized case. The factor of $1/2$ derives from the average $1/2$ chance of each qubit starting in the excited state. The factor of n due to n qubits decaying is an important aspect of interpreting measured T_1 and T_2 times. Dynamics that are less than fully localized will start to show effects of the diffusive case described below.

Between the localized and diffusive cases, another interesting case is the decay of a uniform superposition state, where all n qubits are in $|+\rangle$ states which are unentangled relative to the computational basis. The fidelity is a product of the single-qubit fidelities. This may look like a simple model of a diffused state since the probability has spread to all states equally, but a general diffused state would also be entangled with random, independent phases on each of the 2^n states. The uniform superposition state is then a useful test of the relative roles of spreading probability versus entanglement in quantum state diffusion. Only half of the single-qubit fidelity decays, similar to the averaging factor of one half in the localized case. The same Eq. 13 and Eq. 14 apply with

$$\nu_{\text{single}} = (\nu_1 + \nu_2)/4 = 1/(2T_2). \quad (16)$$

In the diffusive case the Hamiltonian evolution becomes important, but for the QSM we have found it can be abstracted away to simplify the problem and still produce predictions that agree well with simulation. To simplify, note that chaotic mixing occurs on faster time scales than Lindblad decay. Then the density matrix can be expected to quickly reach a randomly entangled pure state of uniformly spread probability, after which the Hamiltonian evolution has little qualitative effect aside from rapidly changing the precise values of the phases. Fidelity decay during diffusive dynamics can then be approximated as the decay of this random pure state under Lindblad evolution. Averaging over initial conditions contributes to an averaging over these random phases, causing the phase-dependent terms in f to vanish. Inspecting $f = \sum_{i,j} \sigma_{i,j} \rho_{i,j}^*$ shows that only $\sigma_{i,j}$ terms that retain their initial phase from $\rho_{i,j}$ survive due to phase cancellation in f . Surprisingly, this causes the qubits to effectively disentangle for off-diagonal terms $\sigma_{i,j} \rho_{i,j}^*$, in a manner describable by two pieces: a non-trace-preserving single-qubit decay and a trace-preserving correction. Along the n -qubit diagonal the flat $\rho_{i,i} = 1/2^n$ causes relaxation effects

across $\sigma_{i,i} \rho_{i,i}^*$ to cancel out. This leaves only effects from dephasing and off-diagonal relaxation, where the random phase averaging removes the gain to lower states but not the loss from higher states. The exact fidelity expression for the diffusive case is provided in Eq. 53 in Appendix C, but its initial decay rate using Eq. 14 is simply

$$\begin{aligned} \nu_{\text{single}} &= \nu_1/2 + \nu_2/4 \\ &= 1/(4T_1) + 1/(2T_2) \geq 1/(2T_1), \end{aligned} \quad (17)$$

which is strictly faster than both the localized and superposition cases when the decay rates are non-zero. Random entanglement combines the effects of full dephasing and partial relaxation for a decay rate that is larger than for any unentangled case when $\nu_1 \sim \nu_2$.

Figure 2 compares the full analytic fidelity evolution for each dynamical case. Each fidelity has the expected feature of starting with an exponential decay that gradually relaxes to the uniformly mixed value of $1/N$. In superconducting qubits the ν_2 rate often dominates, so three types of dynamics are compared for that case in Fig. 2(b). These fidelity decay rates do not account for the gate implementation used in experiment, which is partly rectified in the next section.

2.3.3 Gate-based Lindblad model

The theoretical expressions for the localized and diffusive dynamical cases can now be modified to a gate-based form to better match experimental observations that the majority of errors occur during certain specific gates. Since two-qubit gates are the dominant source of error on IBM-Q, one can model circuit error to lowest order as solely being due to the two-qubit gates causing an enhanced Lindblad decay for each of the target qubits. Averaged over the possible two-qubit subsystems on which the gates act during a circuit, this is approximately described by the dynamics-dependent expressions previously derived, with number of qubits set to two. If the gates are performed serially then the serial gate-based fidelity $f_{\text{GB,S}}(t, n)$ can be given in terms of the dynamics-dependent expressions for the Lindblad fidelity $f_{\text{L}}(t', n')$ as

$$f_{\text{GB,S}}(t, n) = (f_{\text{L}}(1/M, 2))^{Mt} (1 - 1/2^n) + 1/2^n \quad (18)$$

where M is the number of gates per map step, $t = 1$ is the time to complete a map step,

and $1/M$ is the time per gate. Note the late-time (average) fidelity should always approach $1/2^n = 1/N$. For large M the Lindblad expression simplifies to $f_L(t \ll 1, n) \approx e^{-n\nu_{\text{single}}t}$, so

$$f_{\text{GB,S}}(t, n) \approx e^{-2\nu_{\text{single}}t}(1 - 1/2^n) + 1/2^n. \quad (19)$$

This model will be seen in Sec. 4 to qualitatively match experimental results for $n = 3$. Compared to a model that assumes three decaying qubits, when fit to experimental data this gate-based model measures ν_1 and ν_2 that are about $3/2$ larger.

Performing some gates in parallel would increase the average number of simultaneously targeted qubits to $n_{\text{eff}} \leq n$ and decrease gate depth to $D = 2M/n_{\text{eff}}$. Then the fidelity would be

$$f_{\text{GB,P}}(t, n_{\text{eff}}) = (f_L(1/D, n_{\text{eff}}))^{Dt}(1 - 1/2^n) + 1/2^n. \quad (20)$$

For large M this simplifies to

$$f_{\text{GB,P}}(t, n_{\text{eff}}) \approx e^{-n_{\text{eff}}\nu_{\text{single}}t}(1 - 1/2^n) + 1/2^n. \quad (21)$$

Since the physical map step time T_{step} is $n_{\text{eff}}/2$ times shorter for the parallel case compared to serial, the two cases yield the same exponential rate. This just reflects the fact that total fidelity is the product of gate fidelities when gate error is much greater than idle error.

To test the theoretical predictions of Eq. 18 and 20, we use QuTiP's [29] master equation solver. To partially mimic a circuit model we simulate the four unitary steps of Eq. 24 sequentially, rather than simulating the whole Hamiltonian at once. This turns out to be especially important for the localized case, as described below. For the three-qubit simulation we also mimic two-qubit gates by only applying Lindblad operators to two qubits at a time, alternating the qubit pairs [0,1] and [1,2] to mimic the near-linear connectivity on many IBM-Q devices. This matches the effective two-qubit decay rate from theory.

The simulation results in Fig. 3 require a modified interpretation of the theory, as shown for three qubits with serial gates and six qubits with parallel gates. In the localized case, a straightforward Hamiltonian simulation would keep the state localized during the whole map step and would fit well to the theoretical localized decay. But decomposing the evolution to sub-

steps (or further to gates) reveals that the quantum Fourier transforms (QFTs) take the localized state to and from a highly entangled state during half of each map step. This highly entangled state is not fully randomly entangled like a fully diffusive state, yet the simulation results in Fig. 3 for $k = 0.1$ fit well to a half-localized, half-diffusive model where the QFT-transformed state is assumed to decay at the same rate as a diffusive state, forming a map step fidelity of $f_{\text{semi-loc}} \approx f_{\text{loc}}(t/2)f_{\text{dif}}(t/2) \approx (f_{\text{loc}}f_{\text{dif}})^{1/2}$. This implies a semi-localized decay rate given by

$$\nu_{\text{single}} = \nu_1/2 + \nu_2/8. \quad (22)$$

With this modified theoretical prediction, the difference between localized simulation and semi-localized theory is small. One cause of the remaining difference in Fig. 3 is the small non-zero k , which localizes to several neighboring states rather than just one, creating some diffusion and entanglement that enhance the fidelity

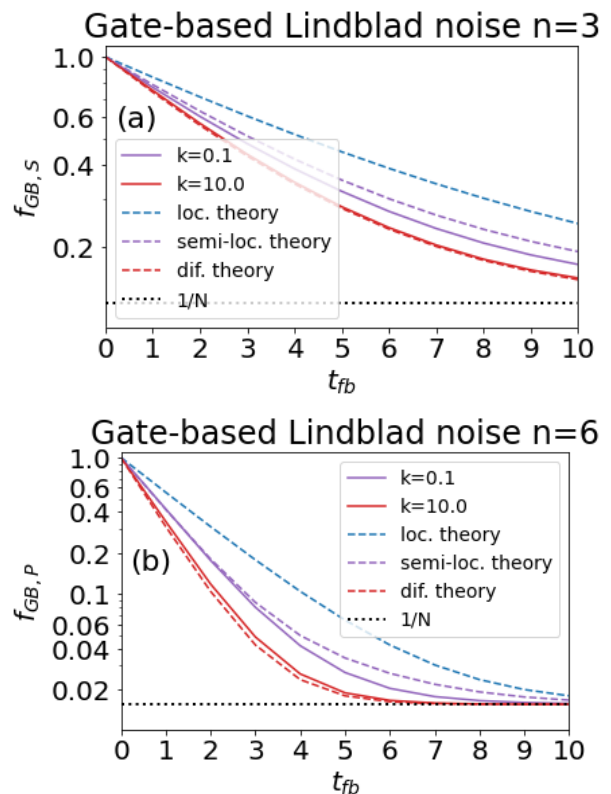


Figure 3: Comparing Lindblad evolutions from full simulation (solid) to the theoretical steady state approximation (dashed) for the fully localized (blue), semi-localized (purple, $k = 0.1$) and fully diffusive (red, $k = 10.0$) cases. Using $\nu_1 = 0.1$ and $\nu_2 = 0.2$. (a) $n = 3$ ($n_{\text{eff}} = 2$) and (b) $n = 6$ ($n_{\text{eff}} = 6$).

decay rate. For $n = 3$ this accounts for $\geq 50\%$ of the difference for $t_{\text{fb}} \geq 5$, but for $n = 6$ it explains only 12% of the difference at $t_{\text{fb}} = 5$. This suggests the fidelity difference between a randomly diffused state and the QFT of a localized state grows as n and t_{fb} increase.

In the diffusive case the difference between theory and simulation is generally smaller despite neglect of the exact Hamiltonian evolution. This suggests that the effect of the precise Hamiltonian evolution on the fidelity is subdominant.

While this model only includes error from two-qubit gates, it could be modified to include other gates. The largest correction would come from idle gates for idling qubits, which have their own decay rates ν_1 and ν_2 . Idle gates are important because CNOT gate error comes primarily from the duration of the gate, implying that any qubit idling in parallel with a CNOT is experiencing a significant fraction of the error. For more details see Sec. 3.2.2 for gate specifics and Table 3 for experimental fits.

2.3.4 IBM Aer gate-based Lindblad simulator

IBM offers several options for artificial noisy simulators. One option is their device-specific noise models [30] which are calibrated to each device's reported errors. Reported T_1 and T_2 times and per-gate error rates from randomized benchmarking are used as input for a combined relaxation, dephasing, and depolarization error model. However, because these models are not customizable, they cannot be fit to experimental data.

We instead use a custom IBM Aer noise model. Closest to our gate-based Lindblad model is a simple Aer model based on the function `thermal_relaxation_error` with parameters T_1 and T_2 and an effective temperature that we set to zero (the default option) [31]. This function applies a single-qubit Lindblad decay to each qubit targeted by a gate based on the duration of the gate, after the gate is done. When $T_2 > T_1$ it applies Kraus operators, but when $T_2 < T_1$ as is common it probabilistically applies single-qubit gates instead. We modify this function to always apply Kraus operators. This model will be used in Fig. 9 to compare the relative importance of specifying the full gate dynamics as in Aer versus simplifying to the four unitary substeps Eq. 24 as in the gate-based Lindblad model.

2.3.5 Effects of parameter noise

Hamiltonian noise models have been studied widely in the quantum maps literature [32, 33, 6, 34, 35, 7, 20, 36, 37, 19], with noise in a parameter being a common variant. Hamiltonian noise models use unitary Markovian errors representing low-frequency or coherent noise. In this section, we study the model of Ref. [6, 35, 7] in which Hamiltonian evolution is perturbed stochastically at each discrete map step by $k \rightarrow k + \Delta k$. The noise Δk is drawn from a normal distribution with standard deviation σ , where the PDF is given by

$$p(\Delta k) = \frac{1}{\sqrt{2\pi}\sigma} e^{-\frac{\Delta k^2}{2\sigma^2}}. \quad (23)$$

This model is discussed more thoroughly in Ref.[1]. This produces a similar effect as the fixed Hamiltonian perturbation discussed in Ref. [19], which itself resembles static coherent noise. Coherent noise can be divided into a component that is consistent over many gates, which can often be fixed through calibration, and a component that varies, which is more difficult to address. The latter resembles parameter noise.

When this parameter noise model is used, the initial conditions $|p\rangle = |0\rangle, |-N/2\rangle$ are excluded from simulations because their symmetry with respect to the map causes their noise-averaged fidelity to asymptotically approach $2/N$ rather than $1/N$. This effect can be misleading on small systems so is avoided here for clarity.

In the presence of random parameter noise, the fidelity of a chaotic map initially decays as $e^{-An_g t}$ with Fermi golden rule $A \sim \sigma^2$ for noise magnitude σ and n_g gates [20], until the golden rule breaks down for large σ [1]. In the presence of static unitary noise the fidelity initially decays tangent to $e^{-An_q n_g^2 t}$ with $A \sim \sigma^2$ for n_q qubits, but at some fraction of the Heisenberg time this transitions to a faster Gaussian decay of $\ln(f) \sim -t^2$ [20]. Quantum dynamical effects, such as Lyapunov and algebraic decay described below, do not immediately set in, so they do not affect the above initial decay rates.

It was previously shown that in the diffusive regime a minimum of six qubits is needed to observe the fidelity decaying at the Lyapunov exponent rate [1]. However in the localized regime an algebraic decay rate is predicted instead [19, 22, 1]. This effect is shown in the QSM

in Fig. 4(b), close to the predicted $f \propto 1/t$ at intermediate times for dimension $d = 1$ and no time auto-correlation of the noise. Since algebraic decay has less stringent constraints than Lyapunov rate decay, it might be observable on fewer than six qubits, though no fewer than four as discussed below.

For parameter noise $f_{fb}(t_{fb})$ still indicates forward-and-back noise and its Fermi golden rule decay has double the decay rate with respect to map steps, $f_{fb,FGR}(t_{fb}) \approx f_{FGR}(2t)$. But its Lyapunov rate decay has the dependence $f_{fb,Lyap}(t_{fb}) \approx e^{-\lambda t_{fb}} = e^{-\lambda t} \approx f_{Lyap}(t)$, showing no increased rate [1]. A similar effect cannot be tested for in algebraic decay, since after fitting the initial fidelities $f_{alg}(t \gg 1) = f_0 t_0/t$ and $f_{alg}(2t \gg 1) = f_0 2t_0/2t$ are equivalent.

Since the diffusive and localized cases have different qualitative behavior under parameter noise, a fidelity gap between the two should appear. This might be confused with the effect of Lindblad noise in a sufficiently noisy experiment, so it is important to check when algebraic decay might occur. Simulations with only parameter noise show a gap is only observed on four or more qubits. On three qubits the gap is in fact reversed, with diffusive fidelity decaying slightly more slowly than localized fidelity. This is demonstrated in Fig. 4(a) where a reversed gap of about 3% (absolute) appears. Interpreting this is complicated by the use of a Gaussian parameter noise distribution which in the case shown causes 2% of map steps to have $k_{eff} = k + \Delta k < 0$, where anomalous diffusion occurs. However the reversed gap persists when anomalous diffusion is avoided with small noise $\sigma \ll k$, so that is not the main cause. A reversed gap or no gap is observed consistently when comparing $0 \leq k \leq 1.9 \approx k_{loc}$ to $k = 20$ at noise values $0 \leq \sigma \leq 1.0$. Comparing the decay rates to $1/t$ suggests that the localized case is still close to algebraic decay, but the diffusive case is limited by the system size to an even slower decay. This result for three qubits suggests the predictions of Lindblad noise are more relevant than parameter noise in present day experiments.

Dynamical localization displays Poisson-like energy spacing statistics, and so indicates locally integrable quantum dynamics, which is the source of the algebraic fidelity decay [19]. But a dynamical fidelity gap can also occur in locally

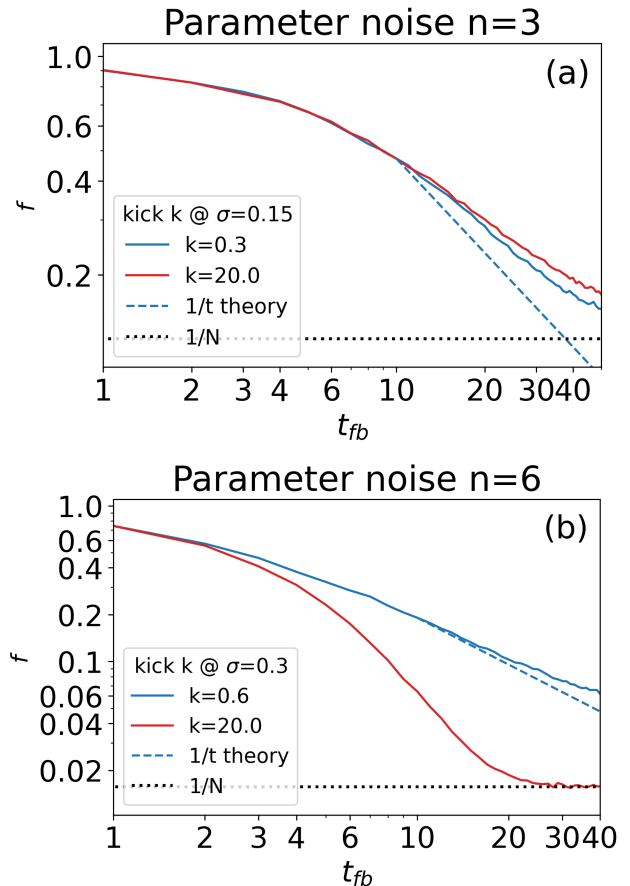


Figure 4: Parameter noise simulations for (a) $n=3$ and (b) $n=6$ on log-log plots to show the algebraic decay rate for localized dynamics. Values of the kick k and Gaussian noise σ are chosen to avoid $k_{eff} = k + \Delta k < 0$ while keeping the number of map steps small. The resulting localized values of k are further from zero due to this. Using 1000 and 100 realizations of the stochastic noise plus 6 and 62 initial conditions for (a) and (b) respectively.

integrable quantum systems such as Ref. [11] (see their Fig. 3).

2.3.6 Combining Lindblad and parameter noise

The theory of Appendix C demonstrates that Lindblad noise by itself does not cause the same qualitative behavior as the parameter noise model; e.g. algebraic decay or exponential decay at the Lyapunov rate. Combining Lindblad and parameter noise can generate these effects, but if the parameter noise is small relative to the Lindblad noise the effects may be difficult to observe.

If the noise processes are statistically independent, then Lindblad and parameter noise fidelities should multiply together. The simulations of the combined noise model in Fig. 5 support this conclusion for both localized and chaotic dynamics. In the chaotic case the rate slows for $1 \leq t \leq 4$ to the product of the Lindblad diffusive rate and the Lyapunov rate, matching pure parameter noise simulations. If the two fidelities instead summed then the slowest exponential rate, namely the Lindblad rate, would dominate by outlasting the others, but that would predict a $3\times$ slower decay than observed. The localized case also supports multiplying fidelities, as during $4 \leq t_{fb} \leq 7$, near the start of $1/t$ decay in Fig. 4, the decay remains faster than either the $1/t$ or semi-localized (Eqs. 21 and 22) analytic decays, rather than one rate dominating. By $t = 8$ the $1/N$ term begins to dominate and slow the decay.

In Ref. [1] three bounds were derived on the observability of Lyapunov decay under parameter noise. However if dynamical and Lindblad noise do have multiplicative effects on the fidelity decay, then one can predict how this noise combination would cause these bounds to change. Bound (1) should remain unchanged, as Lindblad noise likely affects both Fermi golden rule decay and Lyapunov decay equally, causing no change in their competition. Bound (2) should also remain unchanged, as the transition to localization likely occurs at the same parameter value. But bound (3) would tighten, since it describes the limited time steps available to observe Lyapunov decay, which the addition of Lindblad noise would certainly reduce.

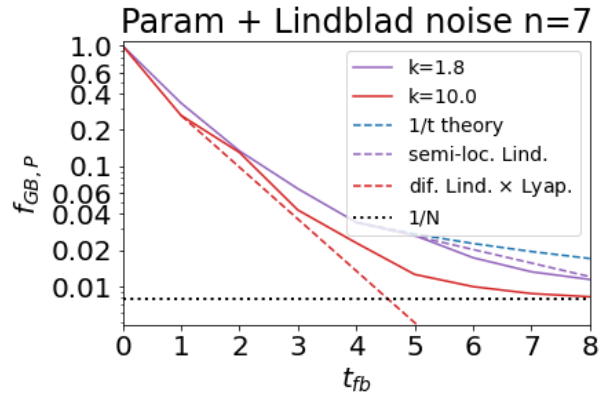


Figure 5: Comparing combined Lindblad and parameter noise simulations (solid) to theory (dashed) for the semi-localized (purple, $k = 1.8$) and diffusive (red, $k = 10.0$) cases. Theory (dashed) includes $1/t$ (blue), Lindblad semi-localized (purple) and the product of Lindblad diffusive and Lyapunov rate decays (red). All results use $n = 7, \nu_1 = 0.025, \nu_2 = 0.05$, and $\sigma = 0.9$. For Lyapunov rate decay, theory assumes $f_{fb, \text{Lyap}}(t_{fb}) = e^{-\lambda t_{fb}}$ as observed.

3 Implementation

3.1 QSM algorithm

There is a natural mapping of the QSM to a qubit-based quantum computer. The N momentum eigenstates can be mapped to the 2^n qubit states when $N = 2^n$. The unitary U_{QSM} can then be implemented exactly in four steps [1, 7, 9], written compactly as

$$U_{QSM} = U_{kin} U_{QFT}^{-1} U_{pot} U_{QFT} \quad (24)$$

where the operators $U_{kin} = U_{phase}(\hbar)$ and $U_{pot} = U_{phase}(-k\beta^2)$ are many-qubit diagonal phase operators in the position and momentum bases respectively, defined in Eq. 2, and U_{QFT} is the quantum Fourier transform used to alternate between the momentum and position bases. The diagonal phase operators can be implemented exactly due to a method for decomposing order- P polynomial terms in the Hamiltonian into P -qubit gates, given in Appendix B [9]. A similar yet approximate algorithm exists for any quantum map whose Hamiltonian has separable kinetic and potential energy terms each with a convergent power series expansion, such as the standard map [9] or kicked Harper model [38]. An exact representation of trigonometric terms requires ancilla qubits. For the U_{QFT} steps we use the standard algorithm from IBM's library, which

is exact, efficient, and requires no ancilla qubits [39, 40].

Using the derivation in Appendix B, the efficient circuit decomposition for the QSM is

$$\begin{aligned}
U_{QFT} &= \prod_{j_1=0}^{n/2-1} \text{SWAP}_{j_1, n-1-j_1} \prod_{j_2>j_1}^{n-1} \text{CP}_{j_1, j_2}(\pi/2^{j_2}) \prod_{j_1=0}^{n-1} \text{H}_{j_1} \\
U_{pot} &= \prod_{j_2>j_1}^{n-1} \text{CP}_{j_1, j_2}(k\beta^2 2^{j_1+j_2}) \times \\
&\quad \prod_{j_1=0}^{n-1} \text{P}_{j_1}(k\beta^2 2^{2j_1-1} - k\beta^2 N 2^{j_1-1}) \quad (25) \\
U_{kin} &= \prod_{j_2>j_1}^{n-1} \text{CP}_{j_1, j_2}(-\hbar 2^{j_1+j_2}) \times \\
&\quad \prod_{j_1=0}^{n-1} \text{P}_{j_1}(-\hbar 2^{2j_1-1} + \hbar N 2^{j_1-1})
\end{aligned}$$

where H is a Hadamard gate and P and CP are one-qubit phase and two-qubit controlled-phase gates respectively. This algorithm is shown for three qubits in Fig. 6. Note the SWAP gates from U_{QFT} have been eliminated just by reversing the order of qubits during U_{pot} .

3.2 IBM-Q Implementation

3.2.1 Circuit optimization

Despite the relative simplicity of the QSM algorithm, executing the circuit in Eq. 25 on IBM-Q’s state-of-the-art hardware quickly accumulates error. Optimizing the circuit to reduce error can greatly improve the results.

We only attempt to reduce error by decreasing the gate count of the two-qubit CNOT gate, the largest-error gate. This is motivated by the goal of benchmarking, which would be complicated by the use of other noise mitigation techniques such as dynamical decoupling. The focus on CNOT gates is motivated by the small total contribution of single-qubit gate errors. According to IBM-Q’s reported RB error estimates, each CNOT gate produces about $30\times$ more error than physical single-qubit gates, namely SX (square-root-of-not) and X gates. (Z gates are virtual with presumably even smaller error [41].) This can partially be attributed to the gate duration, with a CNOT gate taking on average about $10\times$ longer to execute than SX and X gates, which have identical duration. Combining error per gate with the relative

gate counts in Table 1 suggests single-qubit gates contribute no more than 4% of the total error in this context. This remains true for increasing qubit count n per Eq. 25.

To determine the base CNOT gate count of the circuit Eq. 25 on IBM-Q, first logic gates are decomposed to native hardware gates. The simple relations for decomposing are: $\text{PHASE}(\phi) = \text{RZ}(\phi)$ up to an unimportant global phase, where $\text{RZ}(\phi)$ is a Z-rotation by angle ϕ ; $\text{H} = \text{RZ}(\pi/2) \text{SX}$; $\text{RZ}(\pi/2) = \text{CNOT}_{01} \text{CNOT}_{10} \text{CNOT}_{01}$; and lastly the CPHASE gate is given by $\text{CPHASE}_{01}(\phi) = \text{RZ}_1(\phi/2) \text{CNOT}_{01} \text{RZ}_1(2\pi - \phi/2) \text{CNOT}_{01} \text{RZ}_0(\phi/2)$. These decompositions are performed automatically by Qiskit’s `transpile` function.

Reducing the CNOT gate count is done with the gate count optimizer that is automatically applied by the `transpile` function. This does not guarantee optimal results but provides a useful improvement. For this the barriers in Fig. 6 are removed, though barriers between map steps are retained for scalability with number of map steps. Using the above decompositions of each gate on Fig. 6, the base CNOT count on three fully-connected qubits is $12 \times 2 = 24$ CNOT gates. Using `transpile` per Appendix A applies gate transformations stochastically to search for gate reductions. Out of 100 attempts the best optimization reduces gate count from $24 \rightarrow 19$ CNOTs, for a 21% reduction. Smaller gate counts were found, but were for incorrect circuits due to a bug described in Appendix A, or used approximations that did not generalize to other values of k .

Retaining consistent gate count across k is crucial to isolating the effect of dynamics on fidelity decay. This required avoiding specific values of k , such as 2.0 and 4.5, and avoiding $k \ll 2\pi/\beta^2$ where some CP gates in U_{pot} approach identity and the transpiler may eliminate them from the circuit.

Sparse device connectivity increases gate counts, which allows for further gate count optimization. For two unconnected qubits, a CNOT_{02} gate is replaced with $\text{SWAP}_{01} \text{CNOT}_{12} \text{SWAP}_{01}$, transforming one gate to seven. However each CPHASE_{02} gate only needs one pair of SWAPs despite its base decomposition to two CNOT gates. So Fig. 6 before optimization transforms due to linear connectivity from $24 \rightarrow 48$ CNOT gates. Gate optimization over 100 `transpile` attempts reduces from $48 \rightarrow 33$ CNOTs, a 31% reduc-

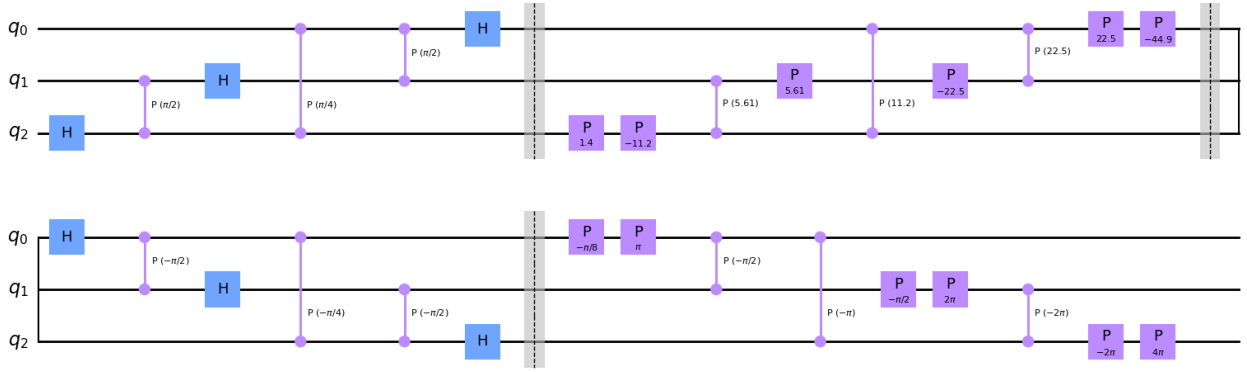


Figure 6: Circuit for a single forward map iteration of the three-qubit QSM algorithm from Eq. 25, before conversion to hardware connectivity and transpilation to native gates. Two-qubit CPHASE gates are used. U_{pot} and U_{kin} steps use PHASE and CPHASE gates, while U_{QFT} steps use CPHASE and H gates. Using $k = 4.55$.

Device, # qubits (connectivity)	(a) # CNOTS (raw Qiskit)	(b) # CNOTs (Eq. 25+Qiskit)	(c) # physical single-qubit gates (Eq. 25+Qiskit)	(d) fidelity $f(1)$ (Eq. 25+Qiskit)
ibmq_manila, n=2	4	4	12-16	0.88-0.90
ibmq_manila, n=3 (linear)	136	66	28-32	0.27-0.37
ibmq_5_yorktown, n=3 (triangular)	82	38	26-30	0.125 (1/N)

Table 1: Native gate counts and fidelity for executing each forward-and-back iteration of the quantum sawtooth map (QSM) experimentally on IBM-Q devices. To calculate forward-only gate counts as for Fig. 7, divide by two. (a) CNOT gate count when Qiskit transpiler attempts direct gate decomposition of the QSM unitary. (b) CNOT gate count when using the efficient algorithm Eq. 25 plus transpiler optimization on linear qubit connectivity. (c) Physical single-qubit gate count, not including virtual RZ gates. Range is over initial condition and dynamical map parameter k . (d) Fidelity as measured by the one-step Loschmidt echo, partly from Fig. 8. Range is over k , varied from diffusive to localizing dynamics, after averaging over initial conditions. Experiment on `ibmq_5_yorktown` performed on October 22, 2020 at 4:41pm EST. Fidelities include measurement error, and at full decoherence reach $1/N$.

tion. The connectivity-caused CNOTs have partially canceled with algorithmic CNOTs, reducing the cost of sparse connectivity.

3.2.2 Circuit scaling

The scaling of circuit error is not very relevant to the three-qubit experiments in this paper, but it is useful for estimating the feasibility of larger simulations, e.g. that could be used to observe the Lyapunov exponent [1]. It is discussed here for completeness in understanding the QSM system as a future benchmarking tool. Gate error is assumed constant for increasing number of qubits, without accounting for error sources like crosstalk which are known to increase the average error per CNOT gate [18]. Moreover, additional scaling may depend on the device under

consideration.

When scaling to more than three qubits, performing CNOT gates in parallel becomes a crucial tool in reducing total error. The degree to which the total circuit error depends on gate *count* versus gate *depth* of parallel gates depends on how the error of a single CNOT gate ϵ_{CNOT} compares to idle error of the same duration ϵ_{IDLE} . If $\epsilon_{\text{CNOT}} = \epsilon_{\text{IDLE}}$, then performing two CNOTs in parallel has identical error as performing a single CNOT with the other qubits idle, meaning performing gates in parallel is a big gain and gate depth determines circuit error. If $\epsilon_{\text{CNOT}} \gg \epsilon_{\text{IDLE}}$, then two CNOTs in parallel have similar error as two in series, meaning parallelization does little and gate count determines circuit error. The model in Sec. 2.3.3 assumed

$\epsilon_{\text{CNOT}} \gg \epsilon_{\text{IDLE}}$ to determine gate-specific error to lowest order. When analyzing circuit scaling, different hypotheses about this relation can lead to a range of results. This combines with uncertainty about how parallelized a circuit is for a total effectiveness of parallelization. This effectiveness reduces error relative to a serial circuit by a factor between one and $n/2$. The relationship between ϵ_{CNOT} and ϵ_{IDLE} is experimentally estimated in Sec. 4.2.2.

To predict the scaling of circuit error due to CNOT gate count and gate depth to many qubits, the previous insights can be combined. Base CNOT gate count from Eq. 25 scales as $O(n^2)$ for n qubits. Worse-case device connectivity (linear) increases this, as the average CNOT requires an extra $O(n)$ SWAPs, each requiring three CNOTs, to connect qubits separated by an average of $O(n)$ connections. Gate count optimization, e.g. using the `transpile` function or similar, may reduce this by up to $O(n)$. Parallelization effectiveness decreases circuit error by between $O(1)$ and $O(n)$ regardless of connectivity. In summary, a circuit with all-to-all connectivity has between $O(n)$ and $O(n^2)$ circuit error scaling due to CNOT gates, and one with linear connectivity has between $O(n)$ and $O(n^3)$ scaling. These ranges depend on the effectiveness of gate count optimization and parallelization. They could be refined by using IBM’s transpiler to see how well CNOT gates parallelize in the QSM across different topologies.

For the gate count optimization performed by `transpile`, it is unknown whether an optimal solution can be found in a scalable fashion. Finding an optimal gate reduction on all-to-all qubit connectivity is an NP-complete problem [42]. In fact even for few qubits with linear connectivity `transpile` struggles to find optimal results. In Table 1 this is demonstrated by comparing the CNOT gate count from the known algorithm Eq. 25 plus optimization in column (b) to a naive approach of compiling the raw unitary U_{QSM} directly in column (a). In each case about one hundred iterations of `transpile` is attempted. For $n = 3$ the naive approach yields over twice the gate count. Whether this suboptimal optimization can provide a scalable benefit is unclear, though focusing on optimizing few-qubit sub-circuits in large algorithms may be the most practical use case.

Since these scalings are all polynomial, they

would all achieve an exponential speedup relative to the $O(n2^n)$ operations required by a classical computer using the fast Fourier transform [7]. However one should keep in mind the scaling of the measurement step, since measuring the entire final state would take an exponential number of runs and destroy the speedup. The speedup is preserved only for measuring collective properties like the Lyapunov exponent [1], localization length, or anomalous diffusion exponent [7].

3.2.3 Choosing a device

At the time of writing IBM-Q freely provides six five-qubit devices, each containing only linear three-qubit sublattices. Among these we choose to test `ibmq_manila` based on its small reported gate error (often $< 6.5\text{E}-3$ on some three-qubit sublattice) and large quantum volume (32). The now-retired five-qubit device (`ibmq_5_yorktown`) had a bow-tie shape with two triangular sublattices but much larger gate error ($> 2.0\text{E}-2$), so we performed experiments on it to explore the trade off between connectivity and gate error. In Table 1 `ibmq_5_yorktown` and `ibmq_manila` are compared, albeit 1.5 years apart, with the latter giving much better performance. Our experiments on `ibmq_santiago` contemporary to the `ibmq_5_yorktown` experiments gave similar results as the more recent `ibmq_manila`, indicating that the time lapse has not had a large effect. A similar result comparing `ibmq_5_yorktown` and `ibmq_santiago` was also found in Ref. [15].

4 Experimental results

4.1 Dynamical localization

One goal of simulating the QSM on present day hardware is to assess the hardware’s ability to execute complex dynamical simulations. In Fig. 7 are the results of simulating the QSM “forward-only” on the `ibmq_manila` device in both the localized and diffusive regimes. The effect of dynamics is clearly apparent, and the localized state’s probability is an informal metric of the fidelity of the quantum hardware. The raw data shows the localized state retains the maximum probability among the eight states through $t = 7$. However Fig. 8’s results for simulating forward-and-back retain fidelity through at least $t_{\text{fb}} = 5$, suggesting the forward-only localized case may

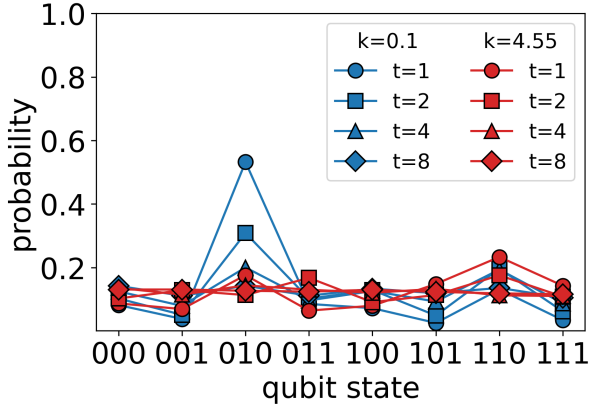


Figure 7: Dynamics of the QSM for three qubits on the `ibmq_manila` device, showing localization ($k = 0.1$) and diffusion ($k = 4.55$) for $t = 1, 2, 4, 8$ and initial condition $p = -2$ ($\psi = |010\rangle$) for best localization. Compare to Fig. 1. Hereafter 8192 experimental shots were taken for each k, t , and initial condition, giving statistical uncertainty $1/\sqrt{N_{\text{shots}}}$. Experiment performed on April 11, 2022 at 10:19pm EST. `ibmq_manila` is re-calibrated every 1-2 hours to adjust for drift that can increase error.

retain information about its initial state through at least $t = 10$.

The metric of the localized state’s probability was used more thoroughly in Ref. [15]. Fig. 7 does not easily compare to Ref. [15] because different map parameters were used, namely $L = 1$ in this work and $L = 7$ in Ref. [15]. This significantly changes the eigenstates, independently of k , and therefore changes the degree of localization. Different parameters were used in the present work to achieve more strongly localized dynamics, as explained in Sec. 2.2.

4.2 Fidelity and dynamics

A more quantitative metric of hardware ability is the Loschmidt echo from Sec. 2.3.1. It measures fidelity as the ability to evolve the system forwards then backwards in time and recover the original state. By choosing simple initial conditions $|\psi\rangle = |p\rangle$ and working in the momentum basis, the initial states are just computational basis states and measuring their final fidelity is just $\langle p | \sigma | p \rangle = \text{Prob}(|p\rangle)$.

By varying the parameter k of the QSM the interaction between experimental noise and dynamics can be measured, as shown in Fig. 8. As predicted by the Lindblad noise model in Sec. 2.3.2, but not the parameter noise model in Sec. 2.3.5 for $n = 3$, localized and diffusive dy-

namics have different fidelity decay rates during the entire simulation. This result shows the existence of this effect in the presence of hardware noise and suggests the Lindblad model can capture this important aspect of three-qubit complex quantum simulation.

Note that for $n = 3, L = 1$ as used here, the predicted transition to full diffusion should occur at $k_{\text{loc}} \approx 1.87$. In the experiment, the largest three k values have indistinguishable decays up to a 1.5% absolute difference despite $k = 1.0$ being below the transition threshold. Further resolution of the observed transition value k_{loc} requires more statistics and larger system size. The smallest three k values show a gradual transition from the strongly localized $k = 0.1$ to the weakly localized $k = 0.45$.

4.2.1 Gate error

The most direct metric for comparing our simulation results to reported metrics from IBM-Q is the CNOT gate error. This does not rely on any models from Sec. 2.3, as it is a single-parameter fit (gate error) for each k . In Table 2 error fits are reported, using just the first time step $f(1)$ and the SPAM error $f(0)$. The fidelity dependence on dynamics is codified here as gate error dependence on dynamics, with a factor of $1.5\times$ in gate error between the extreme dynamical cases.

More interestingly, this range of observed errors is $3.0\text{--}4.5\times$ worse than the error reported by IBM-Q on their online “Systems” screen at the time the experiment was performed [43]. Their reported error comes from standard two-qubit RB with a depolarizing noise model [18]. What causes such a difference between these metrics?

The first suspect is the different dynamics caused by RB Clifford gates and the QSM pseudorandom substeps. Recent research suggests Clifford gates have different quantum scrambling properties than general unitary dynamics: out-of-time-order correlators (OTOCs), which are measures of quantum chaos and scrambling and close relatives of the Loschmidt echo fidelity, reach very different asymptotic values under Clifford and non-Clifford unitary evolution [44, 45]. This may relate to the Clifford group being a 2-design on qudits (and a 3-design on qubits) [44, 46, 47]. Since OTOCs for quantum chaotic systems only grow exponentially until the Ehrenfest time τ_E [48], the QSM which has $\tau_E \sim 1$

	CNOT error (localized)	CNOT error (diffusive)
ibmq_manila reported $n = 2$	5.79E-3	5.79E-3
ibmq_manila experiment $n = 3$	1.76E-2	2.59E-2
ratio of experiment:reported	3.0	4.5

Table 2: Comparison of IBM-Q’s reported RB gate error to error extracted from a three-qubit experiment with localized ($k = 0.1$) or diffusive ($k = 4.55$) dynamics. Experimental error ϵ is calculated from fidelity decay $f(t)$ via $f(1) = (f(0) - 1/2^n)(1 - \epsilon)^{66} + 1/2^n$.

(see Appendix C) saturates quickly. While this is suggestive of a relation between dynamics and fidelity, quantifying the effect is beyond the scope of this paper.

Coherent noise on the hardware could also interact with the dynamics to alter the fidelity decay rate. In Ref. [20] it was shown that in a quantum chaotic map with static Hamiltonian perturbations the fidelity transitions from Fermi golden rule decay to a ballistic Gaussian decay at a fraction of the Heisenberg time. This could further separate the QSM from RB.

Another, better-known suspect is the extra crosstalk from adding a third qubit relative to two-qubit RB. The role of third qubit crosstalk has been investigated with simultaneous RB [18], where average CNOT error per gate was found to increase from $1.63\text{E}-2$ for two-qubit RB to $2.70\text{E}-2$ for 2+1-qubit simultaneous RB, a factor increase due to crosstalk of 1.66. This is surely relevant here, and the factor may vary enough across devices or experiments to wholly explain the error difference of 3.0–4.5. A closer study would be useful for teasing out the size of crosstalk’s contribution.

The effect of dynamics on CNOT error due to Lindblad noise can more fully be captured by a CNOT process matrix tomography experiment. The diffusion and entanglement determine which elements of the process matrix are more strongly enacted in an experiment and therefore which types of error accumulate. The two-parameter gate-based Lindblad model primarily adds a physically-motivated heuristic for the fidelity dependence on dynamics observed in Fig. 8. It provides a balance of utility and efficiency, but sits within the process matrix picture.

The effect of crosstalk goes beyond a static process matrix, as it causes the process matrix to depend on the number of qubits. Both active and spectator qubits can increase error in the CNOT process matrix, meaning even a two-qubit pro-

cess matrix must be measured simultaneously to a variety of gates applied to neighboring qubits in order to correctly predict the fidelity of many-qubit algorithms [18]. The limited connectivity of IBM-Q devices becomes desirable here, as it reduces the number of neighbors per qubit which should limit the magnitude of crosstalk when scaling to many-qubit algorithms. If crosstalk error can be made to saturate at nearest neighbor effects then both characterization and NISQ applications become more feasible.

Considering the contribution of each source to the $3.0\text{--}4.5\times$ larger error is crucial to predicting NISQ quantum advantage. The better each contribution is understood, the more predictive models of error can be constructed.

Lastly, the depolarizing noise model determined through RB is clearly unable to capture or explain the fidelity dependence on dynamics. Its single parameter α_{2Q} of two-qubit gate error measures an average tendency towards the state $\rho = I/N$, rather than capturing important details of how different density matrix elements contribute different rates of decay. Additionally, its focus on averaging over unitary errors, while mathematically convenient, is perhaps less appropriate than single-qubit decoherent errors for describing present day superconducting quantum devices.

4.2.2 Fitting theory to experiment

To compare the experiment of Fig. 8 to the Lindblad theory in Sec. 2.3.2, it is convenient to focus on the extreme cases of $k = 0.1$ and $k = 4.55$. An account of continuously changing k in a Lindblad model and its effect on fidelity would require a careful application of localization length to the Lindblad model, which is beyond the scope of this paper.

Fig. 9 shows numerical fits to experimental fidelity of extreme k for the gate-based

	$T_{1,\text{phys}}$ (μs)	$T_{2,\text{phys}}$ (μs)	ν_1	ν_2
ibmq_manila reported $n = 1$	143	37.4	0.081	0.537
theory fit to experiment $n = 3$	34.6	14.4	0.334 ± 0.016	1.271 ± 0.068
Lindblad simulation fit $n = 3$	90.1	14.3	0.128 ± 0.059	1.486 ± 0.185
Aer simulator fit $n = 3$	250	13.4	0.046 ± 0.019	1.68 ± 0.10

Table 3: Parameter fits from Fig. 9. All values are averaged over three qubits connected in a line on `ibmq_manila`. $T_{1,\text{phys}}$ and $T_{2,\text{phys}}$ values are converted from simulations using $T_{1,\text{phys}} = T_{\text{step}}/\nu_1$ and $T_{2,\text{phys}} = T_{\text{step}} * 2/(\nu_1 + \nu_2)$ where $T_{\text{step}} = 33 * 350\mu\text{s}$. Relaxation ν_1 and pure dephasing ν_2 are dimensionless decay rates per single-direction map step forwards or backwards in time. The analytic theory applies continuous Lindblad decay for two qubits for each of 66 gates per map step. The Lindblad simulation continuously applies Lindblad operators to two qubits in alternating pairs during 8 algorithm substeps. The modified Aer simulator applies Lindblad decay to one and two qubits as Kraus operators after each gate.

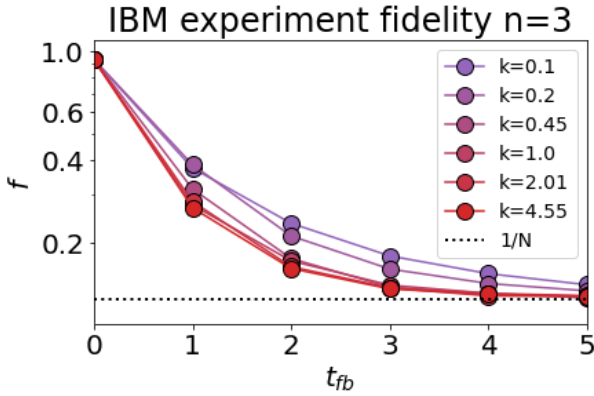


Figure 8: Average fidelity of the QSM on the `ibmq_manila` device for varying k . Localization occurs below $k_{\text{loc}} \approx 1.87$. Data is averaged over all eight initial computational basis states. Statistical uncertainty per data point is $1/\sqrt{8192 * 8} \approx 0.4\%$. Number of CNOT gates per forward-and-back step is $M_{\text{CNOT}} = 66$. The absolute fidelity gap at $t_{\text{fb}} = 1$ between the most localized and most diffusive cases is 10.6%. Experiment performed on January 28, 2022 at 2:44pm EST.

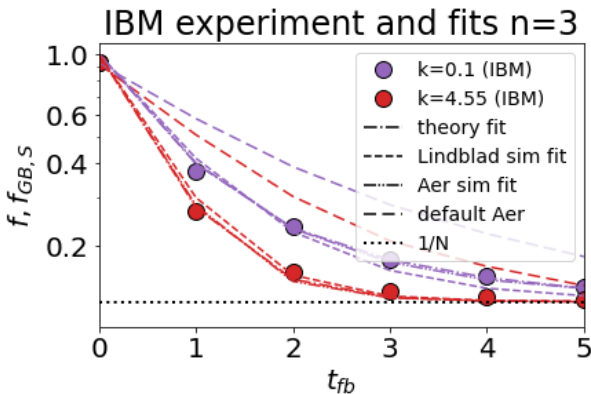


Figure 9: Numerical fits of several models to the data in Fig. 8 for the extreme conditions of localized (purple, $k = 0.1$) and diffusive (red, $k = 4.55$) dynamics. Models described in the main text.

Lindblad theory, the gate-based Lindblad simulations, and an IBM-Q Aer simulator model, all described in Sec. 2.3. Also included is the default Aer model from the function `AerSimulator.from_backend(FakeManila())`, which is designed to fit the error measured by RB.

The default Aer model underestimates error, but the factor difference between its error and observed error is only 1.5 rather than the factor of 3.0–4.5 from Table 2. This is because it draws from a previous device calibration when the relevant gates were 2.0–3.0 \times worse, artificially improving its accuracy. On average it is likely to be less accurate for the three-qubit QSM than shown here.

The Lindblad theory fit uses the gate-based model Eq. 19 with rates Eq. 22 for localized dynamics and Eq. 17 for diffusive dynamics. The Lindblad simulation fit applies single-qubit relaxation and dephasing of uniform rates ν_1 and ν_2 continuously to two out of three qubits, alternating between qubits 0 and 1 or 1 and 2. This is applied during the four unitary steps per Eq. 24 evolved forward-and-back with QuTiP’s `mesolve` function. The Aer simulator fit applies two-qubit and single-qubit gates followed by Kraus operators on the targeted qubits that are determined from decoherence parameters $T_{1,\text{phys}}$ and $T_{2,\text{phys}}$.

These models of fidelity all have just two parameters: ν_1 for relaxation and ν_2 for dephasing, which relate to the physical decoherence times through Eq. 12 and $T_1 = T_{1,\text{phys}}/T_{\text{step}}$, $T_2 = T_{2,\text{phys}}/T_{\text{step}}$. T_{step} is the time to complete a single forward or backward map step on hardware, with $T_{\text{step}} = 33 * 350\mu\text{s}$ to match 33 CNOT gates of average duration $\approx 350\mu\text{s}$ on each of

the forward and backward simulation steps. This only considers time spent in CNOT gates, in accordance with the single-gate-based Lindblad model. The Aer simulator model uses the same T_{step} to convert between parameters, despite including single-qubit gates decaying at the same rate as the CNOT gates, since the single-qubit gates contribute $< 5\%$ to the total duration of gates. Since it directly fits $T_{1,\text{phys}}$ and $T_{2,\text{phys}}$, this extra error is in the converted ν_1 and ν_2 values. Measurement error is neglected in all models, which requires additional parameters to describe the probability of each state being misclassified, and which has small effect on the large exponential decay rates measured here.

The most striking result in Fig. 3 is the consistent values of T_2 across models, as it is also the dominant error source. T_2 measures the decoherence of entanglement, and the QSM with diffusive dynamics produces randomly entangled states (see Appendix C), so it is well-suited to benchmark this noise process.

The variance in ν_2 is larger, but seems to be matched by variance in ν_1 to produce a consistent T_2 . This might be explained by differing weights on ν_1 and ν_2 across models. In Sec. 2.3.2 the theoretical model suggests that during diffusive dynamics, averaging over random phases of entangled states increases the ν_1 contribution to the fidelity decay. This results in ν_1 dominating the decay shared by the localized and diffusive cases and ν_2 being the sole cause of difference between the cases. However three qubits is a small system and has poor random phase averaging, which could alter the relative roles of ν_1 and ν_2 . This might explain the difference between the analytic theory result and the results of the two noise simulations. While the simulation fits are more trustworthy in this case, for larger system sizes the simplified theoretical model should converge more closely to the simulation results.

The average T_2 fit of the three models is $14.0\mu\text{s}$, which is $2.7\times$ smaller than the reported single-qubit idle T_2 time from IBM-Q. This is mostly attributable to larger pure dephasing rate ν_2 , with an average value 1.48 that is $2.8\times$ larger than reported. The T_1 and ν_1 fit values are less consistent, though this is due mostly to the small values of ν_1 being close to zero and therefore being similar in magnitude to the error bars, making them difficult to resolve. In particular the

observed T_1 from the Aer simulator fit is larger than the reported idle value, casting some doubt on the model’s accuracy with respect to T_1 .

The difference between observed and reported values for T_2 is less surprising than the difference in CNOT gate error. The value of measuring this effective CNOT T_2 is to provide a more realistic coherence time for digital quantum simulations and explain heuristically the fidelity dependence on dynamics. It is also a useful test of the question posed in Sec. 3.2.2: How does the error of a CNOT gate ϵ_{CNOT} compare to the error of an idle gate of the same duration ϵ_{IDLE} ? Since the effective CNOT T_2 time dominates the error and is $2.7\times$ shorter than the idle time, this suggests $\epsilon_{\text{CNOT}} \sim 3 \times \epsilon_{\text{IDLE}}$. This is right in between the limits of $\epsilon_{\text{CNOT}} = \epsilon_{\text{IDLE}}$ and $\epsilon_{\text{CNOT}} \gg \epsilon_{\text{IDLE}}$, suggesting the benefit of gate parallelization must be treated carefully when scaling to larger systems.

Note that IBM-Q reports a T_2 value measured by the Hahn echo T_{2E} . This experiment is less sensitive to “inhomogeneous broadening”, that is low-frequency fluctuations that can cause large differences from trial to trial [28]. Since $T_{2E} \geq T_2$, comparing our smaller T_2 fits from running an algorithm to IBM-Q’s larger reported T_{2E} may overstate the difference between CNOT T_2 and idle T_2 , which would suggest a difference factor less than 2.7.

5 Conclusion

In this study an important relationship between the dynamics of a digital quantum simulation and its fidelity under Markovian noise was illustrated. Incoherent Lindblad noise was shown to produce a particularly strong effect in the few-qubit experiments that are currently possible. As the dynamics are changed from localized, to diffusive but unentangled, to diffusive and entangled, the corresponding fidelity decays at an effective T_1 rate, an effective T_2 rate, and a combined rate that is faster than either, respectively.

A Lindblad model with single-qubit noise processes was used to predict this effect, and several related models were used to fit an experimental demonstration. They contain far less information than full process tomography, but more than a depolarizing noise model. This type of physically motivated model is ideal for capturing the effects of dynamics at minimal experimental cost.

To connect to the circuit model, Lindblad noise was assumed to only occur during CNOT gates, which have the largest error. This retains the expected fidelity dependence on gate count while expanding the gate error model from one parameter to two (T_1 and T_2). When further details of the unitary gate decomposition were included, it was found that the dynamics within a simulation time step did have a large impact on fidelity. However the difference between decomposing a time step into four unitary substeps versus the 60+ single- and two-qubit hardware gates was relatively small.

From experiment, first the average error per CNOT gate was estimated. Due to the fidelity dependence on dynamics, the average error varies by a factor of $1.5\times$ over the dynamics. The observed error is $3.0-4.5\times$ greater than reported by IBM-Q’s method of randomized benchmarking with a depolarizing noise model. This discrepancy is largely due to the increase in crosstalk error from two qubits to three. However, how much the different dynamics between RB and the QSM contribute to this error difference is not yet clear.

All models that were fit to experiment agree well on the effective T_2 time, which is dominant, but diverge on the T_1 time, which has a weaker effect and is difficult to resolve. The effective CNOT T_2 time is $2.7\times$ shorter than that of an idle qubit, suggesting a $\sim 3\times$ larger error than an idle gate for diffused states.

Retrieving useful experimental fidelities for complex Hamiltonian simulation was enabled by the highly efficient gate decomposition of the quantum sawtooth map (QSM). It combines the exactness of quantum maps, which do not require Trotterization, with the efficient algorithm for low-order polynomial Hamiltonians. On IBM-Q the QSM required only 33 CNOT gates per evolution time step and 66 CNOT gates per fidelity time step. This enabled seven time steps of clearly localized dynamics and five time steps of forward-and-back fidelity decay.

A model of low-frequency parameter noise was also studied that is relevant to future experiments on more qubits. This model was previously used to show a minimum of six qubits is required to observe the Lyapunov exponent in the QSM. Here it was combined with Lindblad noise to show that the Lyapunov exponent can still be observed, but

will require seven or more qubits depending on the strength of Lindblad noise.

The existence of a large fidelity gap between different dynamics in digital quantum simulations also raises the question of whether arbitrary algorithms may have dynamics that affect their fidelity. In particular, the degrees of entanglement, superposition, and randomness during an algorithm could suggest particular fidelity dependence on the effective T_1 and T_2 . This could be crucial for anticipating quantum advantage by better extrapolating limited device characterization to predict the fidelities of NISQ algorithms.

6 Acknowledgements

The authors thank the Quantum Leap group at LLNL for stimulating discussions and ideas that improved the manuscript, including Vasily Geyko, Frank R. Graziani, Stephen B. Libby, and Yuan Shi. We also thank Jonathan L. DuBois, Kristin M. Beck, Alessandro R. Castelli, and Yaniv J. Rosen of the Quantum Coherent Device Physics group at LLNL, Kyle A. Wendt of the Nuclear Data and Theory group at LLNL, and Robert Tyler Sutherland at UT San Antonio for their insights into quantum hardware and noise processes.

This work was performed by LLNL under the auspices of the U. S. DOE under Contract DE-AC52-07NA27344 and was supported by the DOE Office of Fusion Energy Sciences “Quantum Leap for Fusion Energy Sciences” project FWP-SCW1680 and by LLNL Laboratory Directed Research and Development project 19-FS-078.

References

- [1] Max D Porter and Ilon Joseph. Observability of fidelity decay at the Lyapunov rate in few-qubit quantum simulations. *arXiv preprint arXiv:2110.07767*, 2021.
- [2] Ryan Babbush, Jarrod R McClean, Michael Newman, Craig Gidney, Sergio Boixo, and Hartmut Neven. Focus beyond quadratic speedups for error-corrected quantum advantage. *PRX Quantum*, 2(1):010103, 2021.
- [3] Sergio Boixo, Sergei V Isakov, Vadim N Smelyanskiy, Ryan Babbush, Nan Ding, Zhang Jiang, Michael J Bremner, John M

- Martinis, and Hartmut Neven. Characterizing quantum supremacy in near-term devices. *Nature Physics*, 14(6):595–600, 2018.
- [4] Frank Arute, Kunal Arya, Ryan Babbush, Dave Bacon, Joseph C Bardin, Rami Barends, Rupak Biswas, Sergio Boixo, Fernando GSL Brandao, David A Buell, et al. Quantum supremacy using a programmable superconducting processor. *Nature*, 574(7779):505–510, 2019.
- [5] Ryan Babbush. Google quantum summer symposium 2021: Google’s perspective on the viable applications of early fault-tolerant quantum computers. <https://www.youtube.com/watch?v=-fcQt5C2XGY&list=PLp02pyKis0jL7JdCjzMe0Y1w3TnwTkBT-&index=16>, 2021. Accessed: 2021-09-27.
- [6] Giuliano Benenti and Giulio Casati. Quantum-classical correspondence in perturbed chaotic systems. *Physical Review E*, 65(6):066205, 2002.
- [7] Giuliano Benenti, Giulio Casati, and Simone Montangero. Quantum computing and information extraction for dynamical quantum systems. *Quantum Information Processing*, 3(1):273–293, 2004.
- [8] David Poulin, Robin Blume-Kohout, Raymond Laflamme, and Harold Ollivier. Exponential speedup with a single bit of quantum information: Measuring the average fidelity decay. *Physical Review Letters*, 92(17):177906, 2004.
- [9] Bertrand Georgeot and Dima L Shepelyansky. Exponential gain in quantum computing of quantum chaos and localization. *Physical Review Letters*, 86(13):2890, 2001.
- [10] Asher Peres. Stability of quantum motion in chaotic and regular systems. *Physical Review A*, 30(4):1610, 1984.
- [11] Nathan K Lysne, Kevin W Kuper, Pablo M Poggi, Ivan H Deutsch, and Poul S Jessen. Small, highly accurate quantum processor for intermediate-depth quantum simulations. *Physical Review Letters*, 124(23):230501, 2020.
- [12] Lukas M Sieberer, Tobias Olsacher, Andreas Elben, Markus Heyl, Philipp Hauke, Fritz Haake, and Peter Zoller. Digital quantum simulation, trotter errors, and quantum chaos of the kicked top. *npj Quantum Information*, 5(1):1–11, 2019.
- [13] Markus Heyl, Philipp Hauke, and Peter Zoller. Quantum localization bounds trotter errors in digital quantum simulation. *Science Advances*, 5(4):eaau8342, 2019.
- [14] Michael K Henry, Joseph Emerson, Rudy Martinez, and David G Cory. Localization in the quantum sawtooth map emulated on a quantum-information processor. *Physical Review A*, 74(6):062317, 2006.
- [15] Andrea Pizzamiglio, Su Yeon Chang, Maria Bondani, Simone Montangero, Dario Gerace, and Giuliano Benenti. Dynamical localization simulated on actual quantum hardware. *Entropy*, 23(6):654, 2021.
- [16] Robin Blume-Kohout, John King Gamble, Erik Nielsen, Jonathan Mizrahi, Jonathan D Sterk, and Peter Maunz. Robust, self-consistent, closed-form tomography of quantum logic gates on a trapped ion qubit. *arXiv preprint arXiv:1310.4492*, 2013.
- [17] Erik Nielsen, Kenneth Rudinger, Timothy Proctor, Antonio Russo, Kevin Young, and Robin Blume-Kohout. Probing quantum processor performance with pygsti. *Quantum Science and Technology*, 5(4):044002, 2020.
- [18] David C McKay, Sarah Sheldon, John A Smolin, Jerry M Chow, and Jay M Gambetta. Three-qubit randomized benchmarking. *Physical Review Letters*, 122(20):200502, 2019.
- [19] Philippe Jacquod and Cyril Petitjean. Decoherence, entanglement and irreversibility in quantum dynamical systems with few degrees of freedom. *Advances in Physics*, 58(2):67–196, 2009.
- [20] Klaus M Frahm, Robert Fleckinger, and Dima L Shepelyansky. Quantum chaos and random matrix theory for fidelity decay in quantum computations with static imperfections. *The European Physical Journal D-Atomic, Molecular, Optical and Plasma Physics*, 29(1):139–155, 2004.
- [21] Eliot Kapit. The upside of noise: engineered dissipation as a resource in superconducting

- circuits. *Quantum Science and Technology*, 2(3):033002, 2017.
- [22] Fernando M Cucchietti. The loschmidt echo in classically chaotic systems: Quantum chaos, irreversibility and decoherence. *arXiv preprint quant-ph/0410121*, 2004.
- [23] Heinz-Peter Breuer, Francesco Petruccione, et al. *The theory of open quantum systems*. Oxford University Press on Demand, 2002.
- [24] Isaac L Chuang and Michael A Nielsen. Prescription for experimental determination of the dynamics of a quantum black box. *Journal of Modern Optics*, 44(11-12):2455–2467, 1997.
- [25] Kyle Wendt. Private communication, January 2022.
- [26] Dima Shepelyansky. Scholarpedia: Ehrenfest time and chaos. doi:10.4249/scholarpedia.55031, 2020. Accessed: 2022-05-20.
- [27] Jan Šuntajs, Janez Bonča, Tomaž Prosen, and Lev Vidmar. Quantum chaos challenges many-body localization. *Physical Review E*, 102(6):062144, 2020.
- [28] Philip Krantz, Morten Kjaergaard, Fei Yan, Terry P Orlando, Simon Gustavsson, and William D Oliver. A quantum engineer’s guide to superconducting qubits. *Applied Physics Reviews*, 6(2):021318, 2019.
- [29] J Robert Johansson, Paul D Nation, and Franco Nori. Qutip: An open-source python framework for the dynamics of open quantum systems. *Computer Physics Communications*, 183(8):1760–1772, 2012.
- [30] Device backend noise model simulations. https://qiskit.org/documentation/tutorials/simulators/2_device_noise_simulation.html, 2021. Accessed: 2021-11-01.
- [31] IBM. Source code for thermal relaxation error. https://qiskit.org/documentation/_modules/qiskit/providers/aer/noise/errors/standard_errors.html#thermal_relaxation_error, 2021. Accessed: 2022-05-05.
- [32] Philippe Jacquod, Peter G Silvestrov, and Carlo WJ Beenakker. Golden rule decay versus lyapunov decay of the quantum loschmidt echo. *Physical Review E*, 64(5):055203, 2001.
- [33] Giuliano Benenti, Giulio Casati, Simone Montangero, and Dima L Shepelyansky. Efficient quantum computing of complex dynamics. *Physical Review Letters*, 87(22):227901, 2001.
- [34] Giuliano Benenti, Giulio Casati, Simone Montangero, and Dima L Shepelyansky. Eigenstates of an operating quantum computer: hypersensitivity to static imperfections. *The European Physical Journal D-Atomic, Molecular, Optical and Plasma Physics*, 20(2):293–296, 2002.
- [35] Giuliano Benenti, Giulio Casati, Simone Montangero, and Dima L Shepelyansky. Dynamical localization simulated on a few-qubit quantum computer. *Physical Review A*, 67(5):052312, 2003.
- [36] Wen-ge Wang, Giulio Casati, and Baowen Li. Stability of quantum motion: Beyond fermi-golden-rule and lyapunov decay. *Physical Review E*, 69(2):025201, 2004.
- [37] Thomas Gorin, Tomaž Prosen, Thomas H Seligman, and Marko Žnidarič. Dynamics of loschmidt echoes and fidelity decay. *Physics Reports*, 435(2-5):33–156, 2006.
- [38] Benjamin Lévi and Bertrand Georgeot. Quantum computation of a complex system: The kicked harper model. *Physical Review E*, 70(5):056218, 2004.
- [39] Michael A Nielsen and Isaac L Chuang. *Quantum Computation and Quantum Information*. Cambridge University Press, 2010.
- [40] Quantum fourier transform. <https://qiskit.org/textbook/ch-algorithms/quantum-fourier-transform.html>, 2021. Accessed: 2021-11-01.
- [41] David C McKay, Christopher J Wood, Sarah Sheldon, Jerry M Chow, and Jay M Gambetta. Efficient z gates for quantum computing. *Physical Review A*, 96(2):022330, 2017.
- [42] Adi Botea, Akihiro Kishimoto, and Radu Marinescu. On the complexity of quantum circuit compilation. In *Eleventh annual symposium on combinatorial search*, 2018.
- [43] IBM. IBM-Q Systems. <https://quantum-computing.ibm.com/services?>

[services=systems&systems=yours](#), 2022. Accessed: 2022-01-28.

- [44] Daniel A Roberts and Beni Yoshida. Chaos and complexity by design. *Journal of High Energy Physics*, 2017(4):1–64, 2017.
- [45] Lorenzo Leone, Salvatore FE Oliviero, and Alioscia Hama. Isospectral twirling and quantum chaos. *Entropy*, 23(8):1073, 2021.
- [46] Zak Webb. The clifford group forms a unitary 3-design. *arXiv preprint arXiv:1510.02769*, 2015.
- [47] Huangjun Zhu. Multiqubit clifford groups are unitary 3-designs. *Physical Review A*, 96(6):062336, 2017.
- [48] Koji Hashimoto, Keiju Murata, and Ryosuke Yoshii. Out-of-time-order correlators in quantum mechanics. *Journal of High Energy Physics*, 2017(10):1–31, 2017.
- [49] Max D Porter. Quantum computing stack exchange question. <https://quantumcomputing.stackexchange.com/questions/23458/qubit-identities-get-swapped-in-ibm-qiskit>, 2021. Accessed: 2022-05-05.

A Optimizing performance of a complex algorithm on IBM-Q

Despite using an efficient algorithm, various difficulties can harm performance. Here are some insights for avoiding pitfalls:

- Optimize for qubit connectivity: Circuits that are transpiled to devices with sparse connectivity will add **SWAP** gates to connect distant qubits. This allows for partial cancellation between the algorithm **CNOT** gates and the swapping **CNOT** gates. The automated approach to this is to use a stochastic transpiler as offered by Qiskit. To enable this level of optimization, first set the `transpile` function’s option `optimization_level` from `=1` (the default) to `=3` (the maximum). Next perform a trial-and-error optimization over the transpiler seed by iterating over the option `seed_transpiler=seed` and looking for the lowest resulting gate count of **CNOTs** using `circ.count_ops()` on the transpiled circuit.

Check that the transpiled circuit produces the expected outcome in a noiseless Aer simulator, due to the bug discussed below. Consider saving the result as seed behavior may change. This procedure does not directly scale to many qubits, but on few-qubit subspaces it may be useful at NISQ scales, and may eventually be automated for real applications.

- Optimize algorithms: Look for small optimizations that can be done by hand. For example the QFT algorithm and its inverse require **SWAP** gates to reverse the qubit ordering. But this can be canceled with the argument `do_swaps=False` and replaced with a free, manual reversal of qubit ordering for gates in between the QFT pair.
- Optimize coherence times: Noise properties of backend devices can drift and worsen from their reported values. IBM-Q routinely recalibrates their systems, adjusting qubit and gate pulse properties to reduce error. Each device is currently recalibrated between hourly and weekly, with time since last calibration reported on each device’s status screen online. Timing experiments to occur soon after calibration can help achieve optimal performance for devices that calibrate less than hourly. Choosing the connected set of qubits with the lowest-error gates is also important and should be repeated after a calibration that re-characterizes them, though these occur less often.
- Avoid bugs: A major bug in Qiskit (as of this publication) causes qubit identities to be swapped at the end of a circuit when transpiled without a measurement, as the measurements absorb swaps even when absent [49]. This causes problems when repeating an algorithm step as done here, as it is far more efficient to transpile a single iteration (without measurement) and repeat it rather than transpile a many-iteration circuit all at once. Since this error occurs stochastically, the transpiled circuit should be carefully checked for correct final qubit identities. Seeds that produce incorrect identities can be avoided, or corrective **SWAP** gates may

be added and even re-transpiled to undo the error.

B Gate decomposition of polynomial Hamiltonian evolution

The first step in converting the operators of Eq. 2 into a series of common two-qubit gates is knowing how to implement \hat{p} or \hat{q} (which have identical form in their respective bases). Representing a single-body *state* of quantum number $p' = 0, \dots, N-1$ on $n = \log(N)$ qubits can be accomplished via the binary representation [9]

$$|p'\rangle \rightarrow p' = \sum_{j=0}^{n-1} \alpha_j 2^j \rightarrow |\alpha_{n-1} \dots \alpha_0\rangle \quad (26)$$

where $\alpha_j = 0$ or 1 for each qubit j depending on the value of p' . One can express *diagonal operators* similarly. The operator $U_{p'} = e^{-i\hbar\hat{p}'^2/2}$ can be expressed in the p' basis by noting

$$\begin{aligned} p'^2 &= \sum_{j_1, j_2} \alpha_{j_1} \alpha_{j_2} 2^{j_1+j_2} \quad \text{and so} \quad (27) \\ e^{-i\hbar p'^2/2} &= \prod_{j_1, j_2} e^{-i\hbar \alpha_{j_1} \alpha_{j_2} 2^{j_1+j_2-1}} \\ &= \prod_{j_1} e^{-i\hbar \alpha_{j_1}^2 2^{2j_1-1}} \prod_{j_1 \neq j_2} e^{-i\hbar \alpha_{j_1} \alpha_{j_2} 2^{j_1+j_2-1}} \end{aligned} \quad (28)$$

$$\begin{aligned} e^{-i\hbar\hat{p}'^2/2} &\rightarrow \left[\begin{pmatrix} 1 & & \\ & e^{-i\hbar 2^{2n-3}} & \\ & & \ddots \end{pmatrix} \otimes \dots \otimes \begin{pmatrix} 1 & & \\ & e^{-i\hbar 2^{-1}} & \end{pmatrix} \right] \times \\ &\left[\bigotimes_{j_1}^{n-2} I \otimes \begin{pmatrix} 1 & & \\ & 1 & \\ & & \ddots \\ & & & 1 \\ & & & & e^{-2i\hbar 2^0} \end{pmatrix} \right] \times \dots \end{aligned} \quad (29)$$

This describes PHASE gates on every qubit j_1 and CPHASE gates on every pair of qubits j_1, j_2 with phase $-\hbar 2^{j_1+j_2-1}$ (applied twice, for $j_1 > j_2$ and $j_1 < j_2$). Since the desired operator U_{kin} is shifted by $N/2$ from $U_{p'}$, because $p = -N/2, \dots, (N-1)/2$, it gets modified to

$$\begin{aligned} U_{kin} &\equiv U_{phase}(\hbar) = e^{-i\hbar(\hat{p}'-N/2)^2/2} \\ &\sim e^{-i\hbar\hat{p}'^2/2} e^{i\hbar N\hat{p}'/2} \end{aligned} \quad (30)$$

with unobservable global phase neglected. This contributes further PHASE gates described by

$$e^{i\hbar N\hat{p}'/2} = \prod_j e^{i\hbar N\alpha_j 2^{j-1}}. \quad (31)$$

This describes the U_{kin} gate, but the U_{pot} gate is identical in its own basis with \hbar replaced by $-k\beta^2$ and \hat{p} by \hat{q} with the same $q' = 0, \dots, N-1$:

$$\begin{aligned} U_{pot} &\equiv U_{phase}(-k\beta^2) = e^{ik\beta^2(\hat{q}'-N/2)^2/2} \\ &\sim e^{ik\beta^2\hat{q}'^2/2} e^{-ik\beta^2 N\hat{q}'/2}. \end{aligned} \quad (32)$$

Switching between bases as in Eq. 24 is needed to execute both U_{kin} and U_{pot} with this efficient decomposition. The full algorithm is converted to gates in Eq. 25.

C Fidelity decay of localized and diffusive dynamics under Lindblad noise

C.1 Fidelity of pure states

The quantum sawtooth map exhibits dynamics that range from localized to diffusive (chaotic). To study its interaction with Lindblad noise from a theoretical standpoint, we can make some reasonable simplifying assumptions. The main assumption is that decay of an evolving density matrix is approximately the decay of a pure state with distribution and entanglement typical of the evolving state. In the localized limit this is exactly true. In the diffusive case this requires that the initial evolution to a typical diffusive state is fast relative to Lindblad decay and that after a typical diffusive state is reached the ongoing Hamiltonian evolution can be neglected. The goal is to calculate the fidelity of the decaying state relative to the initial pure state over time. The pure state assumption allows a simplified form. First the general fidelity of corrupted density matrix σ relative to pure state density matrix ρ is

$$f = \left(\text{Tr} \sqrt{\sqrt{\rho} \sigma \sqrt{\rho}} \right)^2. \quad (33)$$

But a pure state has the nice property that

$$\rho^2 = |\psi\rangle \langle \psi| \psi\rangle \langle \psi| = \rho = \sqrt{\rho} \quad (34)$$

which simplifies the fidelity to

$$\begin{aligned} f &= \langle \psi | \sigma | \psi \rangle \\ &= \sum_{i,j} \sigma_{i,j} \rho_{j,i} = \sum_{i,j} \sigma_{i,j} \rho_{i,j}^*, \end{aligned} \quad (35)$$

the Frobenius inner product of the density matrices. It will be useful to consider the elements of the Hadamard element-wise product

$$(\sigma \circ \rho^*)_{ij} = \sigma_{i,j} \rho_{i,j}^* \quad (36)$$

which has elements that sum to the fidelity.

C.2 Localized dynamics

The quantum sawtooth map has a limit of localized dynamics at $k \rightarrow 0$. In this limit the Hamiltonian becomes a diagonal phase matrix $H = \text{diag}(H_0 H_1)$. This only evolves the off-diagonal elements $\rho_{i,j}$ of the density matrix ρ , as seen on a single-qubit example

$$[H, \rho] = \begin{pmatrix} 0 & (H_0 - H_1)\rho_{01} \\ (H_1 - H_0)\rho_{10} & 0 \end{pmatrix}. \quad (37)$$

If we assume an initial state in the computational basis $\rho = \text{diag}(0 \dots 1 \dots 0)$ then the Hamiltonian evolution has no effect on ρ .

C.2.1 Single-qubit decomposition

The effect of Lindblad noise on the localized state can be trivially decomposed into single-qubit effects, since both the Lindblad operators and density matrix decompose.

The Lindblad equation Eq. 11 in the main text describes the noisy time evolution of initial state ρ , with Lindblad collapse operators for T_1 relaxation and T_φ pure dephasing processes [28] on qubit j being

$$L_{1,j} = I \otimes \dots \begin{pmatrix} 0 & 1 \\ 0 & 0 \end{pmatrix} \dots \otimes I \quad (38)$$

$$L_{2,j} = I \otimes \dots \begin{pmatrix} 0 & 0 \\ 0 & 1 \end{pmatrix} \dots \otimes I \quad (39)$$

respectively. For a single unentangled qubit, the solution σ to the Lindblad equation when H has no effect evolves as

$$\dot{\sigma} = \begin{pmatrix} \nu_1 \sigma_{11} & -\frac{\nu_1 + \nu_2}{2} \sigma_{01} \\ -\frac{\nu_1 + \nu_2}{2} \sigma_{10} & -\nu_1 \sigma_{11} \end{pmatrix}. \quad (40)$$

with decay rates that obey $\nu_1 \equiv 1/T_1$, $\nu_2 \equiv 1/T_\varphi$, and $\nu_1/2 + \nu_2/2 = 1/T_2$. Solving this differential equation is simple, as three of the elements depend only on themselves, yielding exponential decays, and the σ_{00} element determined by trace preservation $\text{Tr}(\sigma) = 1$.

Localization simplifies both σ and the fidelity calculation. If the qubit starts in $|\psi\rangle = |1\rangle$, then

$$\sigma = \begin{pmatrix} 1 - e^{-\nu_1 t} & 0 \\ 0 & e^{-\nu_1 t} \end{pmatrix} \quad (41)$$

and $f = \sigma_{11} = e^{-\nu_1 t}$. If it starts in $|\psi\rangle = |0\rangle$ then $f = 1$. No off-diagonal terms means no ν_2 dependence.

C.2.2 Average fidelity

It is useful to average the localized fidelity over all initial conditions for comparison to the diffusive case later. The fidelity for n qubits decomposes into the product of single-qubit fidelities since both ρ and $L_{i,j}$ decompose. j excited qubits then decay at an exponential rate $-j\nu_1$. Averaging over initial conditions includes n states decaying at $-\nu_1$, (n choose 2) states decaying at $-2\nu_1$, and so on. These sum to

$$\begin{aligned} f_{ave} &= \frac{1}{2^n} \sum_{j=0}^n \binom{n}{j} e^{-j\nu_1 t} \\ &= \left(\frac{1 + e^{-\nu_1 t}}{2} \right)^n \\ &\approx 1 - \frac{n}{2} \nu_1 t + O(n^2 \nu_1^2 t^2) \\ &\approx e^{-n(\nu_1/2)t}. \end{aligned} \quad (42)$$

The single-qubit decay rate is seen to be $-\nu_1/2$, as expected.

C.3 Diffusive dynamics

In the other limit of the quantum sawtooth map, large k leads to chaotic, diffusive dynamics. Hamiltonian evolution now has an effect, but will be simplified by two assumptions.

The first assumption is that the fast Hamiltonian evolution reaches a fully diffused state quickly enough to be considered immediate, so that the analysis begins with a randomly entangled state. To justify this, there are two relevant time scales for the initial wave function spreading: the Ehrenfest time τ_E and the Heisenberg time τ_H (see Sec. 2.2). The Ehrenfest time is how long the quantum dynamics closely match the classical dynamics [26]. For a chaotic system this implies rapid spreading at the rate $e^{\lambda t}$. This must end after reaching the finite system size N . This implies an Ehrenfest time of $\tau_E \sim \ln(N)/\lambda$.

To avoid localization $K \gtrsim N^{-2/5}$ when $L = 1$, implying $\lambda \gtrsim N^{-1/5}$ and a bound on Ehrenfest time of $\tau_E \lesssim \ln(N)N^{1/5}$. For small system sizes this is clearly small, and simulations suggest $\tau_E \sim 1$.

Between the Ehrenfest time and Heisenberg time a much slower diffusion occurs. But after the Heisenberg time the effects of quantum interference are fully realized and dynamical localization occurs, halting diffusion. The Heisenberg time for localization is $\tau_H \sim \ell$ [7, 26], which if extended to the diffusive regime suggests $\tau_H \gtrsim N$. Since the Ehrenfest time represents the bulk of the spreading and occurs on a short time scale, this justifies the assumption of an immediate fully diffused state.

The second assumption is that Hamiltonian evolution after full diffusion has little effect on the fidelity decay and can be neglected to simplify the Lindblad evolution. This assumption is supported by numerical simulation results in Fig. 3.

A “typical” diffused state will be considered, with random features to be averaged over. This diffused state is statistically independent of the initial state before Hamiltonian evolution, so an explicit averaging over initial conditions will not be needed. While both amplitudes and phases should be random, a further simplification is to assume that the amplitudes are nearly uniform after the diffusive process occurs, leaving only random phases. This assumption is justified by ergodicity of the dynamics.

After these simplifications, a diffusive state is characterized by two features: statistically uniform probability distribution and random entanglement.

C.3.1 Unentangled state

To test uniform probability and random entanglement independently, first consider a uniform state that is not entangled. Such a state is constructed by initializing in the ground state and applying a Hadamard gate to each qubit. In this case one can again decompose to single-qubit evolution Eq. 40, but acting on initial state

$$|\psi\rangle = \frac{1}{\sqrt{2}}(|0\rangle + |1\rangle)$$

$$\rho = \frac{1}{2} \begin{pmatrix} 1 & 1 \\ 1 & 1 \end{pmatrix}. \quad (43)$$

The Lindblad solution for initial condition ρ is

$$\sigma = \frac{1}{2} \begin{pmatrix} 2 - e^{-\nu_1 t} & e^{-\frac{\nu_1 + \nu_2}{2} t} \\ e^{-\frac{\nu_1 + \nu_2}{2} t} & e^{-\nu_1 t} \end{pmatrix}. \quad (44)$$

The fidelity is again the product of single-qubit fidelities, with each qubit contributing $f = \frac{1}{2} \sum_{i,j} \sigma_{i,j} = \frac{1}{2}(1 + e^{-\frac{\nu_1 + \nu_2}{2} t})$ where exponentials on the diagonal cancel. The n -qubit fidelity for any initial condition is

$$f = \left(\frac{1 + e^{-\frac{\nu_1 + \nu_2}{2} t}}{2} \right)^n$$

$$\approx e^{-(\nu_1/4 + \nu_2/4)t} \quad (45)$$

which is the same form as the averaged localized case Eq. 42, but with $\nu_1 \rightarrow \frac{\nu_1 + \nu_2}{2}$.

C.3.2 Entangled states

In a highly entangled diffusive state, the phases of each n -qubit basis state would be random, preventing decomposition to single qubits. This means

$$|\psi\rangle = \frac{1}{\sqrt{2^n}} \left(|\dots 00\rangle + e^{i\phi_1} |\dots 01\rangle \right. \\ \left. + e^{i\phi_2} |\dots 10\rangle + \dots \right) \quad (46)$$

$$\rho = \frac{1}{2^n} \begin{pmatrix} 1 & e^{-i\phi_1} & e^{-i\phi_2} & \dots \\ e^{i\phi_1} & 1 & e^{i(\phi_1 - \phi_2)} & \dots \\ e^{i\phi_2} & e^{i(\phi_2 - \phi_1)} & 1 & \dots \\ \vdots & \vdots & \vdots & \ddots \end{pmatrix} \quad (47)$$

The fidelity $f = \sum_{i,j} \sigma_{i,j} \rho_{i,j}^*$ shows these phases cancel out at $t = 0$ when $\sigma(t = 0) = \rho$, giving $f = 4^n/4^n = 1$. But how does an n -qubit σ evolve?

Similarly to Eq. 40, the equation for a given $\dot{\sigma}_{i,j}$ will have a relaxation term $-\nu_1 \sigma_{i,j}$ for each qubit that is 1 in both states i and j , a gain term $\nu_1 \sigma_{i+2^k, j+2^k}$ for each qubit that is 0 in both states i and j where k is that qubit’s index in the list of qubits, and a dephasing term $-\frac{\nu_1 + \nu_2}{2} \sigma_{i,j}$ for each qubit that is 0 in i or j but 1 in the other. With only the gain term coupling the matrix elements, and only along the same diagonal, it is straightforward if time-consuming to solve the set of equations on each diagonal of σ . Then the elements of $\sigma \circ \rho^*$ can be summed to calculate the fidelity.

Two qubits It is instructive to work out the fidelity for two qubits. The main diagonal terms have the simplest contribution, since $\sum \sigma_{i,i} \rho_{i,i} = \sum \sigma_{i,i} / 2^n = 1/2^n$ due to trace preservation $\text{Tr}(\sigma) = 1$. The precise dynamics on the diagonal are irrelevant for the diffusive fidelity, as was seen even in the unentangled state.

For off-diagonal terms, many high-index elements of σ do not have gain terms, making them simple exponential decays. For two qubits,

$$\begin{aligned} \dot{\sigma}_{2,3} &= -\frac{\nu_1 + \nu_2}{2} \sigma_{2,3} - \nu_1 \sigma_{2,3} \\ \sigma_{2,3} &= \frac{1}{2^n} e^{i(\phi_2 - \phi_3)} e^{-\frac{3\nu_1 + \nu_2}{2} t} \end{aligned} \quad (48)$$

where the indices correspond to binary states, i.e. $2 = 10_2, 3 = 11_2$. This matrix element describes qubit 0 in superposition and qubit 1 in state 1, producing the first and second terms above, respectively. In contrast, a low-index state depends on decay from high-index states:

$$\dot{\sigma}_{0,1} = -\frac{\nu_1 + \nu_2}{2} \sigma_{0,1} + \nu_1 \sigma_{2,3}$$

If we insert the ansatz $\sigma_{0,1} = Ae^{at} + Be^{bt}$ into the equation, then we find

$$\begin{aligned} \dot{\sigma}_{0,1} &= a(Ae^{at} + Be^{bt}) + B(b - a)e^{bt} \\ a &= -\frac{\nu_1 + \nu_2}{2} \\ b &= -\frac{3\nu_1 + \nu_2}{2} \\ B &= \frac{\nu_1}{2^n} e^{i(\phi_2 - \phi_3)} \frac{1}{b - a} = -\frac{1}{2^n} e^{i(\phi_2 - \phi_3)} \end{aligned}$$

with initial condition

$$\begin{aligned} \sigma_{0,1}(t=0) &= A + B = \frac{1}{2^n} e^{-i\phi_1} \\ A &= \frac{1}{2^n} \left(e^{-i\phi_1} + e^{i(\phi_2 - \phi_3)} \right) \end{aligned}$$

giving the solution

$$\sigma_{0,1} = \frac{1}{2^n} \left[\left(e^{-i\phi_1} + e^{i(\phi_2 - \phi_3)} \right) e^{-\frac{\nu_1 + \nu_2}{2} t} - e^{i(\phi_2 - \phi_3)} e^{-\frac{3\nu_1 + \nu_2}{2} t} \right]. \quad (49)$$

In the unentangled limit where all $\phi_i \rightarrow 0$, the fidelity contributions of the two elements $\sigma_{2,3}$ and $\sigma_{0,1}$ partially cancel, eliminating the faster decay. But with random phase entanglement their combined contribution generally doesn't cancel, instead giving

$$\begin{aligned} \sigma_{0,1} \rho_{0,1}^* + \sigma_{2,3} \rho_{2,3}^* &= \\ \frac{1}{(2^n)^2} \left[\left(1 + e^{i(\phi_1 + \phi_2 - \phi_3)} \right) e^{-\frac{\nu_1 + \nu_2}{2} t} + \left(1 - e^{i(\phi_1 + \phi_2 - \phi_3)} \right) e^{-\frac{3\nu_1 + \nu_2}{2} t} \right]. \end{aligned} \quad (50)$$

In the fidelity this is further combined with its complex conjugate, resulting in cosines of the phases.

So the effect of random phases from diffusive entanglement does not change which fidelity decay rates are possible, but rather to change the relative weight of each term. This lesson will generalize to n qubits.

Since Eq. 35 says fidelity is a sum over matrix elements of $\sigma \circ \rho^*$ (Eq. 36), it is helpful to show this full matrix for two qubits:

$$\sigma \circ \rho^* = \frac{1}{4^2} \begin{pmatrix} 4 - 4e^{-\nu_1 t} + \left(1 + e^{i\phi_{123}} \right) e^{-\frac{\nu_1 + \nu_2}{2} t} + \left(1 + e^{i\phi_{123}} \right) e^{-\frac{\nu_1 + \nu_2}{2} t} + e^{-\frac{2\nu_1 + 2\nu_2}{2} t} \\ e^{-2\nu_1 t} \quad \left(-e^{i\phi_{123}} \right) e^{-\frac{3\nu_1 + \nu_2}{2} t} \quad \left(-e^{i\phi_{123}} \right) e^{-\frac{3\nu_1 + \nu_2}{2} t} \quad e^{-\frac{3\nu_1 + \nu_2}{2} t} \\ c.c. \quad 2e^{-\nu_1 t} - e^{-2\nu_1 t} \quad e^{-\frac{\nu_1 + \nu_2}{2} t} \quad e^{-\frac{3\nu_1 + \nu_2}{2} t} \\ c.c. \quad c.c. \quad 2e^{-\nu_1 t} - e^{-2\nu_1 t} \quad e^{-\frac{3\nu_1 + \nu_2}{2} t} \\ c.c. \quad c.c. \quad c.c. \quad e^{-2\nu_1 t} \end{pmatrix} \quad (51)$$

where $\phi_{123} \equiv (\phi_1 + \phi_2 - \phi_3)$. The diagonal matrix elements only have terms for relaxation to lower states and gain from higher states. Off-diagonal terms also have dephasing due to superposition

qubits. The number of superposition qubits for an element can be counted from its indices, i.e. element $(\sigma \circ \rho^*)_{2,3}$ measures the superposition between states $2 = 10_2$ and $3 = 11_2$, so only qubit

0 is in superposition between 0 and 1. This contributes one factor of $e^{-\frac{\nu_1+\nu_2}{2}t}$, which combines with the decay term $e^{-\nu_1 t}$ from qubit 1. Off-diagonal gain terms are the only terms for which the random phase factors of σ and ρ^* do not cancel, making them the only way phase dependence enters the fidelity.

n qubits An n -qubit average fidelity can be found based on this two-qubit example. First, when $\nu_1 = 0$ the coupling between elements disappears, eliminating the phase-dependent terms in fidelity. This is just the unentangled case with the solution Eq. 45.

When $\nu_1 \neq 0$ the fidelity $f = \sum_{i,j} \sigma_{i,j} \rho_{i,j}^*$ generally depends on the phases. However we can calculate the *average* fidelity over random phases ϕ_i . The motivation for this phase averaging is twofold. First, the 2^n initial conditions of basis states $\{|p\rangle\}$ are averaged over, with each producing statistically independent phases. Second, even if the phases have some probability distribution with finite variance and zero mean, the number of independent phases that sum in the fidelity grows quickly with number of qubits. Two-qubit fidelity has only one independent phase ϕ_{123} per initial condition and time step, but three-qubit fidelity has four, each appearing with multiple decay rates. As the number of qubits grows, most decay rate coefficients sum over many independent phases, producing an additional effective averaging. Between these two averaging effects over the uniform distribution of phases, the variance of the mean should quickly shrink towards zero.

Some phase-dependent terms will always be controlled by just a few phases, specifically $\sim n$ phases rather than one due to n -fold symmetry in permuting qubit identities. This could break the assumption of phase averaging. However, in the worst case a single such poorly-averaged decay rate coefficient will have fidelity contribution $\sim n/4^n$, so the effect of each will be small, as well as independent.

Assuming then that averaging over each phase gives an approximately correct total fidelity, one can use $\langle e^{i\phi_i} \rangle = 0$ to eliminate phase dependence in the fidelity. This does not reduce to the unentangled case. Off-diagonal elements of $\sigma \circ \rho^*$ lose their gain terms but not their relaxation and dephasing terms. This means probability flow from high to low states retains the loss from high

but not the gain to low. Equivalently, all coupling terms in the differential equations for σ can be dropped, greatly simplifying each matrix element to a single term each. Diagonal elements are not changed by phase averaging since they have no phase dependence, so they retain their gain terms.

The general n -qubit average fidelity can be constructed from this understanding. The fidelity is

$$f = \frac{1}{2^n} + \frac{1}{4^n} \sum_{k=1}^n e^{-k\frac{\nu_1+\nu_2}{2}t} \binom{n}{k} 2^k \sum_{l=0}^{n-k} e^{-l\nu_1 t} \binom{n-k}{l}. \quad (52)$$

This construction goes as follows: First count the diagonal terms as the sum $\frac{1}{2^n}$ due to trace preservation. Then for each off-diagonal term $\sigma_{i,j}$, count the number of qubits k in superposition between states i and j . For k qubits in superposition, the effects of dephasing combine for a decay rate contribution of $-k\frac{\nu_1+\nu_2}{2}$. The number of qubit permutations with k qubits in superposition is $(n \text{ choose } k)$, and there are 2^k ways the superposition qubits can be flipped between matrix index contribution ordering 0, 1 and 1, 0, i.e. matrix element $0, 3 = 000_2, 011_2$ and $2, 1 = 010_2, 001_2$ have the same dephasing rate. These two factors count the number of matrix elements with that dephasing rate. The non-superposition qubits can each be in state 0 or 1, but phase averaging has eliminated gain to 0 while preserving relaxation from 1. This requires a sum over number of excited qubits. Elements with l excited qubits have additional exponential fidelity decay at a rate $-l\nu_1$, and there are $((n-k) \text{ choose } l)$ permutations of these excited qubits. Lastly, since the diagonal elements must be excluded from these sums for not following the same rules after averaging, the index $k=0$ for zero superposition qubits must be removed. It is helpful to subtract this term after the fact.

One validation of Eq. 52 is that it can be easily modified to describe the unentangled case of Eq. 45. When all phases ϕ_i are zero, instead of the gain terms averaging to zero they perfectly cancel the decay terms. To reflect this, remove the effect of decay in Eq. 52 via the replacement $e^{-l\nu_1 t} \rightarrow 1$. The sum over l then evaluates to 2^{n-k} and simplifying recovers Eq. 45.

The full Eq. 52 simplifies to

$$f = \frac{1}{4^n} \left(1 + e^{-\nu_1 t} + 2e^{-\frac{\nu_1 + \nu_2}{2} t} \right)^n - \frac{1}{4^n} \left(1 + e^{-\nu_1 t} \right)^n + \frac{1}{2^n} \quad (53)$$

$$\approx 1 - n(\nu_1/2 + \nu_2/4)t + \frac{1}{2^n} n(\nu_1/2)t + O(n^2(\nu_1/2 + \nu_2/4)^2 t^2) \quad (54)$$

$$\approx e^{-n(\nu_1/2 + \nu_2/4)t}. \quad (55)$$

Comparing this averaged diffusive entangled decay to the diffusive unentangled decay Eq. 45, the effect of ν_1 on the initial rate approximately doubled but the effect of ν_2 remains the same. The extra ν_1 contribution comes from relaxation terms that no longer cancel with gain terms.

The diffusive fidelity Eq. 53 can be understood more intuitively by noting the phase averaging decouples all matrix elements except the n -qubit diagonal. A single decoupled, phase-averaged qubit within the n -qubit system, ignoring the trace preservation from the n -qubit diagonal, can be considered as having a fidelity matrix $\sigma \circ \rho^*$ of

$$\frac{1}{4} \begin{pmatrix} 1 & e^{-\frac{\nu_1 + \nu_2}{2} t} \\ e^{-\frac{\nu_1 + \nu_2}{2} t} & e^{-\nu_1 t} \end{pmatrix} \quad (56)$$

where the gain term has been removed relative to Eq. 44. The fidelity $f = \sum_{i,j} \sigma_{i,j} \rho_{i,j}^*$ of this to the n th power for n qubits forms the first term in Eq. 53. The latter two terms are corrections for the n -qubit diagonal, since the diagonal has no phases to average as is clear from initial state Eq. 47. The second term removes the erroneous diagonal term and the third replaces it with the appropriate $1/2^n$ from trace preservation.